DESIGN AND OPTIMIZATION OF A MARS SAMPLE RETURN MISSION WITH NUCLEAR THERMAL ROCKETS

A Thesis presented to the Faculty of the Graduate School

University of Missouri

In Partial Fulfillment

Of the Requirements for the Degree

Master of Science

By

TYLER M. CHLAPEK

Dr. Craig A. Kluever, Thesis Supervisor

DECEMBER 2011

The undersigned, appointed by the dean of the Graduate School,

have examined the thesis entitled

DESIGN AND OPTIMIZATION OF A MARS SAMPLE RETURN MISSION WITH NUCLEAR THERMAL ROCKETS

Presented by Tyler M. Chlapek

A candidate for the degree of

Master of Science

And hereby certify that, in their opinion, it is worthy of acceptance.

_____

Craig A. Kluever

_____

Douglas Smith

_____

Stephen Montgomery-Smith

DEDICATION

This thesis is dedicated to my parents who, with unending love and support, have given up an insane portion of their lives to insure that I've had opportunities for learning and success.

ACKNOWLEDGEMENTS

Many thanks are owed to my advisor, Dr. Craig A. Kluever, for his guidance throughout the research and thesis-writing processes. His assistance has been invaluable, and this thesis would not have been possible without him.

I would also like to thank Dr. Steven Howe and the Center for Space Nuclear Research for providing the impetus for the project and the means to complete it during two summer fellowships. Also at the Center for Space Nuclear Research, fellows Ross Allen and Brian Manning completed much of the propulsion analysis and mission design work that is presented here.

TABLE OF CONTENTS

LIST OF ILLUSTRATIONS

Figure Page

LIST OF TABLES

NOMENCLATURE

a	=	semi-major axis, km
c	=	chord length, km
$C3$	=	launch energy, km^2/s^2
C_{pen}	=	penalty constant
CR	=	crossover probability
e	=	orbital eccentricity
F	=	differencing weight
g	=	gravity acceleration, km/s^2
G	=	generation
h	=	angular momentum, km^2/s
IMLEO	=	injected mass in low-Earth orbit, kg
I_{sp}	=	specific impulse, s
m	=	mass of smaller body, kg
M	=	mass of larger body, kg
N	=	number of revolutions
NP	=	population size
p	=	semilatus rectum, km
P_S	=	frequency of success
r	=	radius, km
R	=	radial distance between two large bodies, km
t	=	time, s or days
T_0	=	Earth departure date, month/day/year
$T_{95\%}$	=	time to optimize to 95% confidence, s
TOF_1	=	Earth-to-Mars time of flight, days
TOF_2	=	Mars-to-Earth time of flight, days

T_{stay}	=	stay time at Mars, days
T_{trial}	=	time per trial, s
V	=	Velocity, km/s
$\vec{x}$	=	design vector
β	=	*B*-plane offset, km
Γ	=	penalty function
γ	=	flight-path angle, deg
ε	=	tank/propellant mass fraction
η	=	structure mass fraction
θ	=	true anomaly, deg
μ	=	gravitational parameter, km^3/s^2
ξ	=	specific energy, km^2/s^2

DESIGN AND OPTIMIZATION OF A MARS SAMPLE RETURN MISSION WITH NUCLEAR THERMAL ROCKETS

Tyler Chlapek

Dr. Craig A. Kluever, Thesis Advisor

ABSTRACT

Nuclear thermal propulsion (NTP) is recognized as the only solution to human exploration of the near planets during the next several decades, but NTP currently receives little funding for development. In order to foster interest in the technology, a mission architecture is presented that develops and flight-proves NTP on NASA's planned 2018 Mars sample return mission with a relatively low cost of $100 million. In order to facilitate the planning of similar round-trip Mars missions, a Differential Evolution (DE) trajectory optimization program is constructed. DE tuning parameters are systematically studied in order to characterize DE performance and find the best parameter configurations for constrained and unconstrained trajectories. A highly-tuned version of the algorithm is found to globally optimize Mars missions in less than three minutes for 30-year launch windows and less than two minutes for 3-year launch windows.

CHAPTER 1: INTRODUCTION

1.1 Nuclear Thermal Rockets

1.1.1 Operation Principles

Nuclear thermal propulsion (NTP) makes use of the great power output and power density of nuclear reactors. The basic operating principle of a solid-core nuclear thermal rocket (NTR) is that a working fluid, often hydrogen, is pumped through flow channels in the core of a nuclear reactor. In the flow channels, heat is transferred from the core to the fluid such that the fluid reaches temperatures up to 3,000 K by core exit. Upon exit the fluid passes through a converging-diverging nozzle and exits the nozzle with an effective exhaust velocity approaching 9 km/s [1]. Figure 1.1 shows major components of a typical 1960s-era NTR [2].

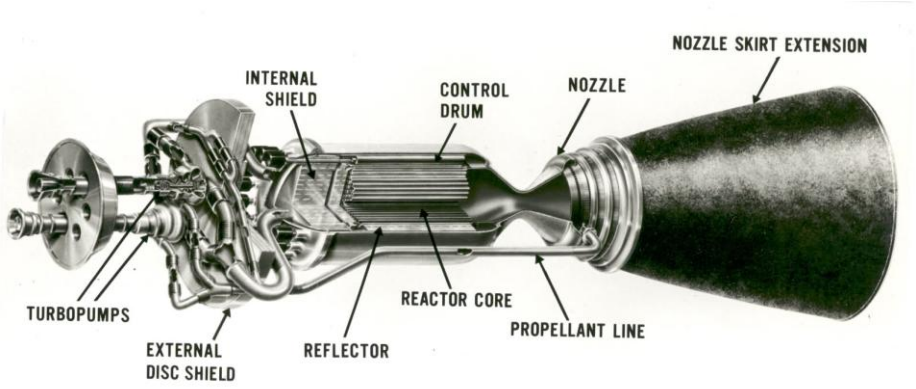

Fig. 1.1 Diagram of 1960s NTR [2].

Two performance criteria typically used to describe propulsion systems are thrust and specific impulse I_{sp}. Specific impulse is a measure of efficiency for propellant systems—the thrust divided by the amount of propellant used per unit time, equivalent to the change in momentum produced per unit mass propellant expended. Higher thrust

values allow fast acceleration for time-limited maneuvers such as manned orbit transfers, and increasing I_{sp} yields more efficient use of propellant.

I_{sp} scales with the square root of exhaust temperature over propellant molecular weight [3]. While high-thrust chemical systems actually have higher exhaust temperatures than NTP, they require oxidation—which results in relatively high-mass propellants—to achieve those temperatures. NTP, on the other hand, can directly heat and use low-mass H_2. Table 1.1 gives the in-space I_{sp} of several notable chemical and nuclear thermal propulsion systems, showing that NTRs use propellant nearly twice as efficiently as the best chemical systems [3].

Table 1.1 Vacuum I_{sp} of several notable propulsion systems [3].

	Manufacturer	Engine	Vacuum I_{sp} (s)
Chemical	Aerojet	AJ110	320
	Pratt & Whitney	RL 10B-2	456
	Rocketdyne	Space Shuttle (main)	426
	Rocketdyne	RS-27A (Delta 2)	302
NTP	NERVA	Pewee	845
	Pratt & Whitney	TRITON (concept)	911

The high temperatures and mass-flow rates achievable with NTRs make them the only propulsion system that is considered simultaneously high specific impulse and high thrust.

1.1.2 Project Rover and the Nuclear Engine for Rocket Vehicle Application Program

More than just a concept, NTRs were proven with flight-certified components during Project Rover from 1955-1972 and the Nuclear Engine for Rocket Vehicle

Application (NERVA) program from 1963-1972. NERVA and Rover ran in parallel—Rover developed graphite-fueled reactors and tested them at low power, and the NERVA program combined the reactors with propulsion hardware to create thermal rockets. Though limited to ground testing, NERVA progressed so rapidly in the 1960s that NASA Marshall Space Flight Center (MSFC) began using NTRs in mission plans with the primary focus on manned Mars missions [4]. By 1968, NERVA had developed NTRs to a Technology Readiness Level (TRL) of 6. The TRL system provides a measure of the maturity of any technology. Levels range 1-9 with TRL 1 corresponding to the initiation of applied research and TRL 9 corresponding to mission-proven technology [5]. TRL 6 is the designation given to a system that has been proven in a relevant environment, fully demonstrating engineering feasibility.

With NTRs designated TRL 6 in 1968, the Space Nuclear Propulsion Office certified that NERVA engines met the requirements for manned Mars missions, and NASA deemed the engines ready for incorporation into a spacecraft. The high cost of the non-propulsive aspects of manned Mars missions became apparent during the early 1970s, however, just as the space race was winding down. With less public support for expensive programs, the Nixon administration was forced to cancel plans for the Mars mission due to budget priorities [6]. NERVA and Project Rover were subsequently terminated in 1972, because the manned mission had been the only near-term application for which NTP was deemed enabling. In all, $1.4 billion in 1972 dollars, or $7.4 billion in 2011 dollars, was invested in the program [4].

The NERVA program was considered a success overall. It accomplished all of its goals and demonstrated the exceptional performance and reliability of NTRs. Several

performance achievements of note are an I_{sp} of 845 s (nearly twice that of today's best chemical propulsion systems), thrust-to-weight—the ratio of engine mass to the thrust produced—of up to 4.8, power levels of up to 4.5 GW, and thrust up to 250 klbf [7]. The stability and reliability of NTRs were demonstrated by 28 restarts and over 1 hour of continuous runtime for a single engine: the operation time during final tests was only limited by the size of the H_2 propellant tank.

1.1.3 Support and Development Since NERVA

Widespread support for NTP has waxed and waned with political shifts since the termination of NERVA, but many in the space community have consistently acknowledged NTP as an enabling technology for human space travel beyond the moon. An Independent Review Panel was convened in 1999 to review propulsion technologies being considered in the NASA Advanced Space Transportation Program [8]. The review panel concluded that fission-based propulsion was the only technology of the 45 presented which was "applicable to human exploration of the near planets in the near to mid-term time frame…." In agreement with the panel's findings, the last three incarnations of NASA's Mars Design Reference Architecture (DRA), versions 3.0, 4.0, and 5.0, have called for the use of NTRs for all in-space propulsion of cargo and crew vehicles due to significant mass advantages [9]. DRA 5.0 was published in 2009 and is the manned mission architecture that NASA currently supports.

Modern mission concept studies such as DRA 5.0 do not employ the original NERVA rockets but instead use contemporary designs that utilize the last several decades' technological advancements in fuel fabrication and power generation [10]. One of the most important developments is the advent of combination ceramic-metallic

"cermet" fuels. Cermet properties allow for higher operating temperatures and therefore higher efficiency thrust. Cermet durability is also greatly superior to graphite and could potentially fix the problem of fuel degradation that occurred in NERVA rockets [11]. Fuel degradation was reduced to an acceptable level by the end of NERVA, but it was one of the program's most problematic issues [4].

Advances in power generation have made the concept of bimodal NTRs more feasible. Bimodal NTRs, as the name implies, are capable of operating in two different modes: propulsion and power. When in power mode, bimodal NTRs use a closed-loop Brayton cycle with the reactor heat to generate modest amounts of power. An example of a modern design is the TRITON by Pratt & Whitney, pictured in Fig. 1.2 [12]. The TRITON is a "trimodal" NTR that can provide high efficiency propulsion with H_2 propellant, high thrust with LOX-augmented H_2 propellant, and electrical power through a closed-loop Brayton cycle.

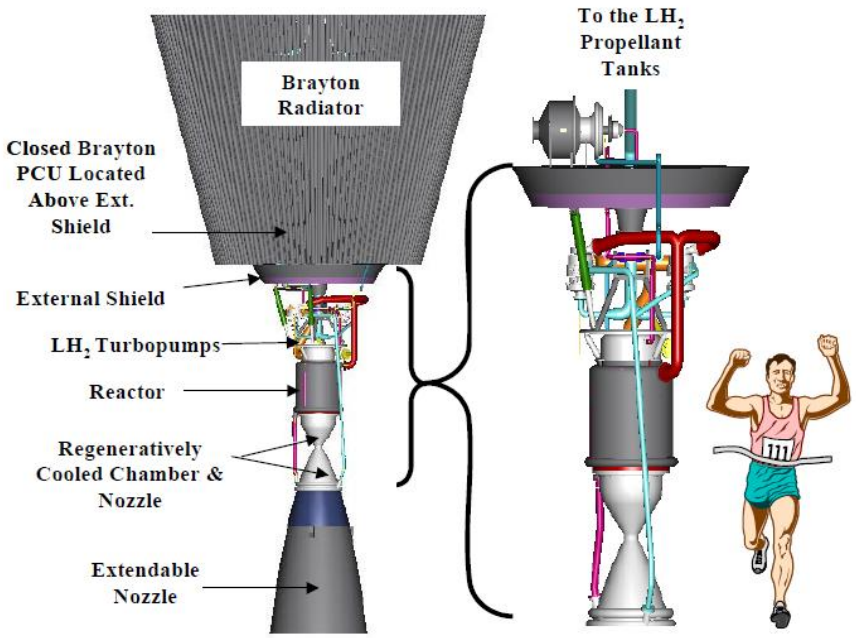

Fig. 1.2 Diagram of Pratt & Whitney "trimodal" Triton NTR [12].

While NTP work since NERVA has almost entirely consisted of paper studies, the last several years have seen initiation of fuel fabrication research at MSFC, Idaho National Lab (INL), and the Center for Space Nuclear Research (CSNR). These efforts are on track to fabricate and test prototypic fuel elements within the next year. Recognizing the necessity of NTP for human space exploration, MSFC and the CSNR are also making strong efforts to devise affordable development and qualification strategies [13,14]. The mission concept presented in this thesis was developed by the CSNR in an effort to create an affordable strategy for near-term development and implementation of NTP.

1.1.4 Affordable NTR Concept

Many NTP critics claim development costs up to $10 billion for the first functional NTR. Instead of building an entirely new rocket design, the CSNR proposes that a useful, low-cost, and functional NTR can be developed and implemented by rebuilding the NERVA Pewee engine with only one major modification—substituting a W-Re cermet fuel for the NERVA graphite. The 500 MW Pewee, tested in 1968 and shown in Fig. 1.3, was the culmination of much of NERVA's research. The W-Re cermet fuel proposed for substitution has been under study at the CSNR for several years, and fuels scientists are on track to fabricate a fuel element loaded with depleted uranium by the end of 2012.

Fig. 1.3 Pewee 2 reactor at Jackass Flats test site.

At 2,570 kg mass, 27 klbf thrust, and specific impulse of 845 s Pewee's performance greatly exceeds that of today's comparably-sized chemical systems. The CSNR is currently in the process of obtaining approximately 1,500 Pewee engineering drawings from Los Alamos National Laboratory, where they have been in storage since NERVA. It is believed that with these drawings, two of which are shown in Figs. 1.4-1.5, the original Pewee components can be rebuilt at relatively low cost.

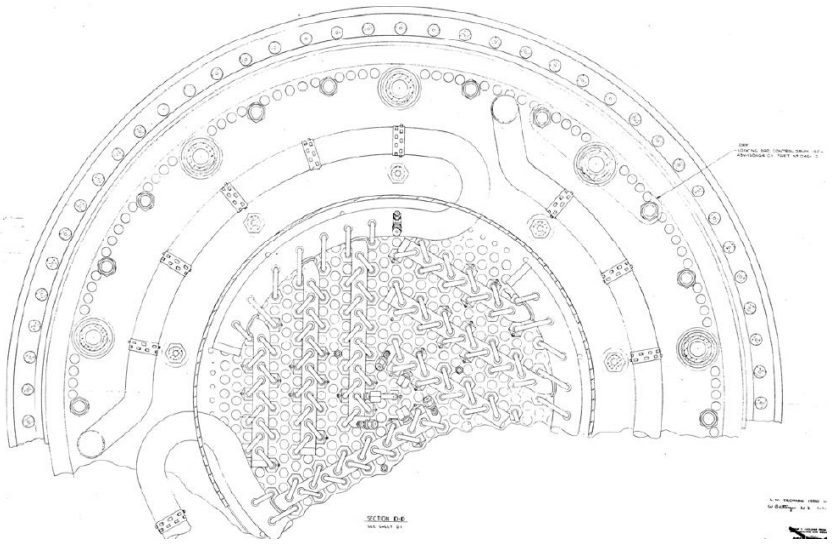

Fig. 1.4 Schematic of top of Pewee core with gas manifolds [15].

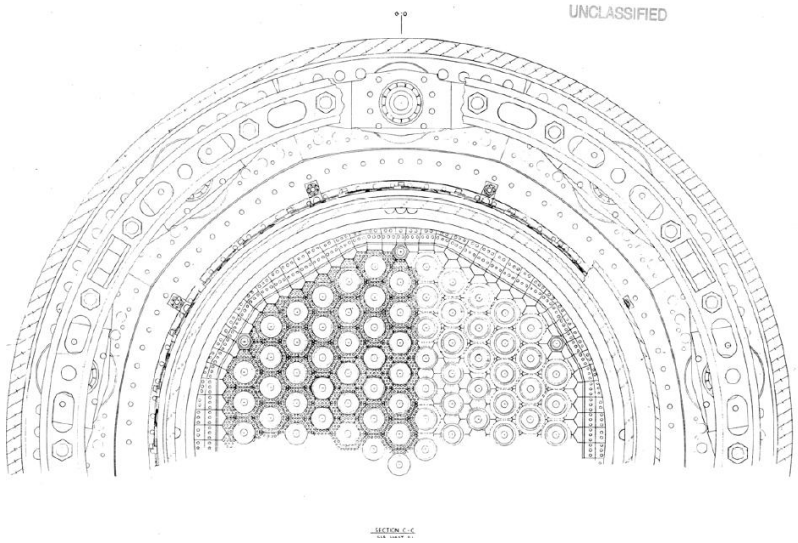

Fig. 1.5 Schematic of bottom of Pewee core with fuel pins and reflectors [15].

The "affordable" NTR strategy, by utilizing the extensive engineering knowledge gained from NERVA, argues that there is only the need to construct one test and one flight engine. Qualification costs for NTR fuel are minimal when compared to terrestrial fuels, because thrust-only NTRs have a total operation time of less than two hours. Engine tests are conducted with the Subsurface Active Filtering of Exhaust (SAFE)

concept [16], shown in Fig. 1.6, in which exhaust gas is contained in bore holes at the Nevada Test Site. The SAFE concept requires $15 million for facility construction and $1.8 million for each test.

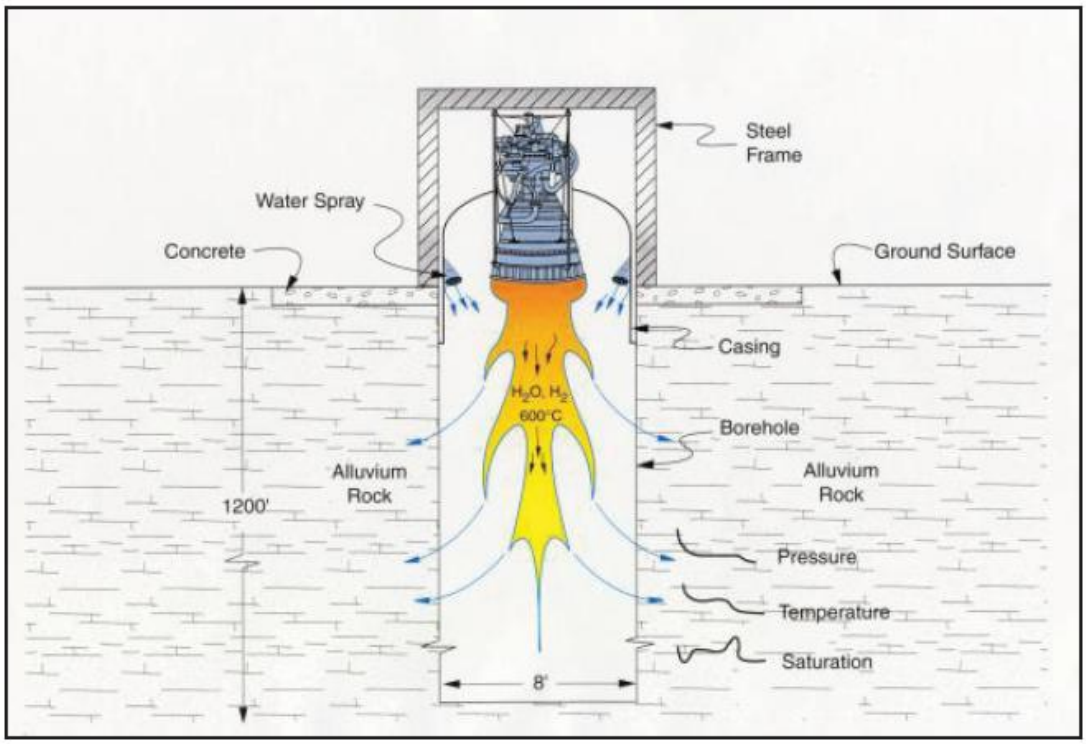

Fig. 1.6 NTR SAFE testing concept [16].

The total projected development, construction, and testing cost with 30% reserves for the two engines is approximately $700 million. Once the first engine is flown in space, the infrastructure established for the development of the affordable NTR can then be used for the development of a more modernized design such as Pratt & Whitney's TRITON for use on larger missions. The proposed development plan is thus a cost-effective means of restarting development of a technology that is necessary for missions with high performance propulsion requirements, i.e. large robotic or manned missions.

1.2 Mars Sample Return

The next major step in the United States' Mars exploration program is to return Martian samples to Earth for analysis. Missions such as Viking, Mars Pathfinder, the Mars Exploration Rovers, Phoenix, and Mars Science Laboratory missions have or plan to analyze samples on the Martian surface, but samples have yet to be returned to Earth for analysis. Returning samples to Earth allows for a virtually unlimited number of tests and much more in-depth analysis than can be performed on Mars. Mars sample return (MSR) is also the next logical step before a manned Mars mission: the current U.S. space policy has the goal of landing humans on Mars by the mid-2030s [17].

Sending a spacecraft to Mars and back requires several major propulsive maneuvers, explained briefly here as they are key to mission architecture planning. First, the entire craft must be launched into a low-Earth orbit (LEO), just above Earth's atmosphere, on a launch vehicle (LV) such as an Atlas V. Once initial system checks are completed in LEO, a large propulsive burn provides the trans-Mars injection (TMI) to put the spacecraft on an intercept trajectory with Mars. If a Mars orbit is the desired target upon arrival at Mars, the craft conducts a Mars-orbit insertion (MOI) burn when it reaches the desired orbital altitude. Alternatively, if the goal is atmospheric entry for landing, the spacecraft can enter directly or perform a burn to slow to the desired entry speed. To leave Mars, a trans-Earth injection (TEI) is conducted in the same manner as TMI. At Earth, the spacecraft enters LEO with an Earth-orbit insertion (EOI) burn, conducts a burn to match the desired entry speed, or enters directly.

The current U.S. MSR plan resulted from the 2010 NASA and NRC Planetary Science Decadal Survey (PSDS). The 2010 PSDS investigated scientific mission

possibilities to bodies of interest in the solar system for pursuit in the 2013-2023 timeframe. The missions studied were required to be, above all, science-driven as well as financially feasible with the projected available funding. Based on these requirements, the PSDS chose MSR as the top priority mission in the next decade [18]. The current MSR mission plan is a joint venture between NASA and the European Space Agency (ESA)—the two organizations are attempting to find a mutually satisfactory strategy to sharing development and launch costs [19]. The mission plan consists of separate launches for three different mission components: 1) a large science rover, 2) an orbiter/return vehicle, and 3) a lander that contains a Mars ascent vehicle (MAV) and small fetch rover. Each package is launched with an Atlas V 531-551 with the first launch in 2018 and the last in 2024 [20]. The total cost of three Atlas V LVs is approximately $750 million.

The planned NASA MSR mission is an ideal candidate for cost-effective, near-term implementation of NTP. This thesis proposes a PSDS-derived architecture that strictly adheres to the PSDS plan except for the methods of Earth launch and TMI. Minimal changes are made to other parts of the mission in order to maximize acceptance from the space community and efficiently utilize the vast analysis completed during original mission planning. The architecture presented here combines the three original spacecraft packages into a single payload for TMI. Instead of performing TMI burns with the Centaur 3rd stage of each Atlas V as specified by original plan, a single TMI burn is performed by a Pewee-derived NTR. The volume and mass of the NTR and its propellant are significantly lower than the combined Centaur stages, therefore reducing the requirements of the Earth LV. Instead of three Atlas V's, the initial ascent from

Earth's surface to LEO is accomplished with a single SpaceX Falcon Heavy. Conservatively estimating $150 million for a Falcon Heavy launch [21], $600 million is saved in launch costs. Thus, launch cost savings cover most of the development costs for a Pewee-derived NTR.

1.3 Interplanetary Trajectory Optimization

Launching payloads into space from Earth's surface is extremely expensive. The Atlas V 551, the largest LV considered in this study, achieves a cost of approximately $13,200 per kilogram for delivering its maximum payload of 18,814 kg to LEO [22]. For spacecraft that require large propulsive maneuvers to depart LEO for other planets or deep-space trajectories, it is common for propellant to make up the majority of the spacecraft mass in LEO. Because propellant is such a large portion of the spacecraft mass, propulsive maneuvers are only performed at the most opportune times when the departure and arrival locations allow for minimum-energy transfers. Propellant mass for these maneuvers can vary greatly with small differences in launch or arrival times: Deviating from the optimum by only a few days can increase the required propellant mass, and thus the injected mass to LEO (IMLEO), by as much as 10-20% for an Earth-to-Mars transfer (as demonstrated in section 6.2). Such an increase can consequently require the use of a larger LV, increase costs by millions of dollars, or make the transfer infeasible until the departure and arrival locations align once more. Depending on the mission, realignment can take years to decades to occur.

Because of the limitations and costs of launching mass into space, space missions of all types require extensive trajectory optimization to find optimal parameters for major

propulsive maneuvers. Further, mission execution requires an extremely high degree of accuracy for all orbital maneuvers, as even slight errors in velocity or targeting can result in complete mission failure through unintended position errors, planetary flyby, atmospheric skip-out, or burn-up during entry. Fortunately, preliminary mission planning can be accomplished with simplified, approximate trajectory models that have greatly reduced computation requirements. This study utilizes the patched-conic method for initial trajectory assessments.

The patched-conic method, as its name implies, reduces the trajectory model to a series of two-body dynamics problems. At any one point in time, spacecraft motion is modeled simply as a Keplerian conic section about a single attracting mass. When the spacecraft leaves the region of gravitational influence of one body and enters that of another, the two conic sections are "patched" together. While such approximations cannot not yield truly accurate results, they are useful for determining approximate launch windows for feasibility assessments and starting points for more detailed optimizations [3].

The functions defining propulsive requirements for Earth-Mars transfers are riddled with local minima over the design space of departure date and time of flight. Earth and Mars have orbits of different periods, eccentricities, and inclinations; consequently, their relative positions and orientations repeat in a synodic period of near-exactly every 79 years [9]. The relative positions repeat less exactly every 15 years and still less exactly every 2.1 years. The 2.1-year periods occur because of the planets' orbital periods about the sun, and the longer periods result because the phase-angle of Mars lags the phase angle of Earth. Propulsive requirements can vary substantially for

each 2.1-year optimum, but these near-optimum solutions have been sufficient for past Mars missions such as the 2003 Mars Exploration Rover (MER), 2005 Mars Reconnaissance Orbiter, 2007 Phoenix, and 2011 Mars Science Laboratory. Figure 1.7 shows the Earth-to-Mars trajectory of the MER Spirit rover, planned at an optimal 2.1-year minimum energy condition. The eccentricities of Earth and Mars orbits are visible.

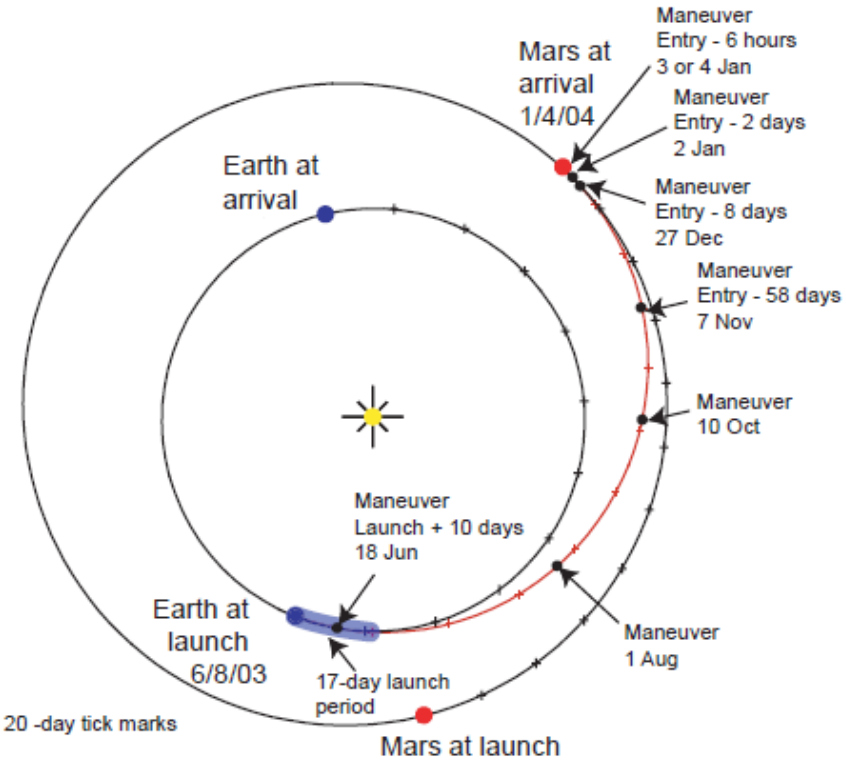

Fig. 1.7 Earth-to-Mars trajectory of MER Spirit rover [23].

The goal of trajectory optimizations in this study is to minimize spacecraft volume and IMLEO, and thus launch costs, for round-trip Mars missions. While numerous past studies provide optimal minimum energy transfer dates and propulsive requirements [24,25,26], it is desired to construct a preliminary design tool that incorporates constraints on trajectory parameters—such as transfer times and entry interface velocities, which are important due to physical limitations of spacecraft and

humans—specific to several different mission architectures. This study builds on previous research, detailed in Section 1.4, and develops an algorithm that efficiently calculates optimal launch dates, flight times, and stay times for round-trip Mars missions. Global optima are found for each synodic period for constrained and unconstrained trajectories, enabling the construction of preliminary mission timelines, mass budgets, and cost estimates.

1.4 Differential Evolution

The algorithm chosen for trajectory optimization is Differential Evolution (DE). Invented by Storn and Price [27] in the mid-1990s, DE is a direct search metaheuristic global optimizer in the evolutionary algorithm family. Requiring no special information or assumptions about a problem prior to optimization, DE has proven practically effective for global optimization of complex, noisy, and discontinuous functions [28]. DE's strengths lie in its population differencing method as well as its relatively simple implementation when compared to similar methods such as Particle Swarm Optimization (PSO) and Genetic Algorithms (GA) [29].

DE was first investigated for use in trajectory optimization in a University of Reading study that was sponsored by the European Space Agency (ESA) [29]. The study investigated the robustness and efficiency of various global optimization algorithms when applied to standard optimization benchmarking functions as well as trajectory problems of differing complexity. The algorithms considered were the deterministic DIRECT and Multi-level Coordinate Search (MCS), the model-based stochastic Probabilistic Global Search Lausanne (PGSL) and Cross Entropy (CE), and the instance-

based stochastic GA, PSO, Multiple Particle Swarm Optimization (MPSO), and DE. The study analyzed three categories of trajectory problems: 1) bi-propulsive interplanetary transfers (BPIT), 2) multiple gravity assist (MGA) trajectories, and 3) MGA trajectories with deep space maneuvers (DSM). Using default tuning parameters for each algorithm, DE proved to be the only algorithm that yielded satisfactory convergence and computation time for all trajectory problems. MCS and MPSO outperformed DE on BPIT and MGA trajectories, respectively, but the authors deemed DE more suitable for further use because of advantages in robustness and ease of implementation.

A second ESA-funded study conducted by the University of Glasgow [30] found DE to have only average performance when compared to algorithms such as Adaptive Simulated Annealing (ASA), Fast Evolutionary Programming, Evolutionary Predictive Interval Computation, and MCS. The discrepancy between the two ESA studies can possibly be explained by the inconsistencies in the DE tuning parameters. It is widely known in the optimization community that algorithm performance can be highly dependent on tuning parameters. This knowledge and the discrepancy between studies serve as motivation for investigation of the effects of optimization algorithms' tuning parameters on trajectory problems.

Olds, Kluever, and Cupples [31] systematically investigated the relationship between DE performance and tuning parameters on various high-thrust trajectory problems that require parking orbit insertion and/or gravity assists. Olds optimized for minimum ΔV, as was done in [29,30], but imposed more rigorous constraints on trajectory parameters. By conducting sets of 1000-run trials for various combinations of tuning parameters the study showed that certain combinations yield rapid convergence

while others never converge to the desired solution. Olds also showed that while some parameters generally perform well, performance varies between different types of problems. The study found that DE tuning parameters do not follow any identifiable pattern and concluded that a probabilistic study of parameters is needed to maximize algorithm performance for each problem.

Sentinella and Casalino [32] developed a hybrid algorithm that runs DE, GA, and PSO in parallel and allows the best individuals to migrate to other populations. In optimizations of rendezvous missions, the hybrid always found optima in fewer function evaluations than the individual algorithms. The hybrid also proved to be more robust through successful optimization with sub-optimal tuning parameters. It is important to note, however, that [32] used a static set of DE tuning parameters and a relatively large population size of 60 for all optimizations. It is possible that by tailoring tuning parameters to each problem and using a more reasonable population size, as in [31], DE could prove to be the more efficient algorithm.

Vinkó et al. [33] benchmarked DE and other global optimization techniques on six different trajectory optimization problems. Popular algorithms such as PSO, GA, ASA, GLOBAL, and COOP (a combination of PSO and DE) were applied to trajectories that require multiple gravity assists and deep space maneuvers. While DE found more optimum solutions than any other algorithm on 3 of 6 problems, it only produced the best average solution on one problem. Vinkó concluded that the COOP combination of PSO and DE gives superior performance on average when compared to standalone solvers. Note again that each algorithm in [33] used a set of non-optimal tuning parameters.

The CSNR has funded the development of a Mars mission trajectory optimization program (MMTOP) for use in preliminary planning of Mars missions of various structures. It is desired to make the algorithm easy to implement and alter for users who are not familiar with numerical methods or interplanetary trajectories. In addition to ease of use, it is desired that the algorithm allow for rapid optimization of trajectory parameters. While it is highly probable that several of the algorithms studied in [29,30,333] could be extremely robust and efficient if tuning parameters are optimized, DE is chosen for its ease of implementation [27,29,31] and evidenced robustness with tailored tuning parameters [31]. Analysis of tuning parameters is carried out similar to [31], but this study focuses solely on round-trip Mars trajectories.

CHAPTER 2: PHYSICAL MODEL

2.1 Major Assumptions

Exact, high-precision spacecraft positions during interplanetary transfers are highly sensitive to small propulsive maneuvers and require direct integration of small perturbing forces such as solar radiation pressure, drag from sparse space matter, and gravity from distant celestial bodies. Accounting for these forces is necessary for detailed mission analysis and execution, as even small errors in velocity direction and magnitude can lead to mission failure. Mission failure in this sense can mean position errors of hundreds of kilometers at the conclusion of a mission or, for missions that require atmospheric entry or orbit insertion, unintended skip-out of atmosphere, burn-up during entry, or planetary flyby. The level of accuracy needed to address these issues requires extremely computationally intensive calculations. Fortunately, this accuracy is not necessary for preliminary mission design.

The model used in this study makes several approximations that greatly reduce computation time. Space is treated as a perfect vacuum, and all celestial bodies are treated as point masses. The patched conic method is adopted for interplanetary transfers. The method of patched conics assumes spacecraft motion occurs as a series of Keplerian conic sections, each one governed by the gravity of a single dominant body. The spacecraft can naturally transfer between regions that have different dominating bodies, so conic sections are "patched" together at boundaries of influence to form a continuous path of motion. It is obvious that such approximations cannot yield completely accurate results, as spacecraft are always under the influence of multiple

celestial bodies; however, this level of accuracy is recognized as necessary and sufficiently accurate for preliminary mission planning and launch window determination [3].

One tool for addressing trajectory errors is found in trajectory correction maneuvers (TCM). Even with the most detailed simulations, planetary missions often require TCM to address targeting errors and unforeseen dynamics perturbations. Propellant contingencies for TCM are built into spacecraft designs, and propulsive burns are performed as needed throughout each mission. Building on this technique, this thesis includes conservative TCM propellant contingencies in spacecraft mass calculations. Provisioning a larger-than-typical TCM propellant mass provides a safeguard against errors from approximate modeling and ensures that estimations of total IMLEO are not unrealistically low.

2.2 Two-Body Motion and Conic Sections

Two-body motion for systems with attracting mass *M* much greater than small-body mass *m*, as is the case for the spacecraft-Sun or spacecraft-planet systems, is governed by

$$\frac{d^2\vec{r}}{dt^2} + \frac{\mu}{r^3}\vec{r} = \vec{0} \tag{2.1}$$

where μ is the gravitational parameter of *M*, and $\vec{r}$ is the vector from *M* to *m*. Equation (2.1), derived from Newton's Law of Universal Gravitation, makes the important implication of the concepts of conservation of energy and conservation of angular

momentum. These two principles make it possible to calculate the position and velocity attributes of *m* at any point in its orbit. The specific energy ξ for a spacecraft is

$$\xi = \frac{V^2}{2} - \frac{\mu}{r} = \frac{-\mu}{2a} \tag{2.2}$$

with velocity magnitude *V*, radius magnitude *r* from *M*, and semi-major axis *a*. The spacecraft velocity vector $\vec{V}$ is simply the time derivative of $\vec{r}$.

$$\vec{V} = \dot{\vec{r}} \tag{2.3}$$

The specific angular momentum is

$$\vec{h} = \vec{r} \times \vec{V} \tag{2.4}$$

in vector form and

$$h = \mu p = rV\cos\gamma \tag{2.5}$$

as a scalar with flight-path angle γ between $\vec{V}$ and the local horizon. Radius magnitude *r* can be calculated with

$$r = \frac{p}{1 + e\cos\theta} \tag{2.6}$$

for any true anomaly θ. True anomaly θ is the angular displacement of the spacecraft from periapsis, the position of closest passage in an orbit, and it is measured in the direction of spacecraft motion. The semilatus rectum *p* is

$$p = a\left(1 - e^2\right) \tag{2.7}$$

where $r=p$ at $\theta=90°$ and $\theta=270°$. Important angular and positional parameters are shown for an elliptical orbit in Fig. 2.1.

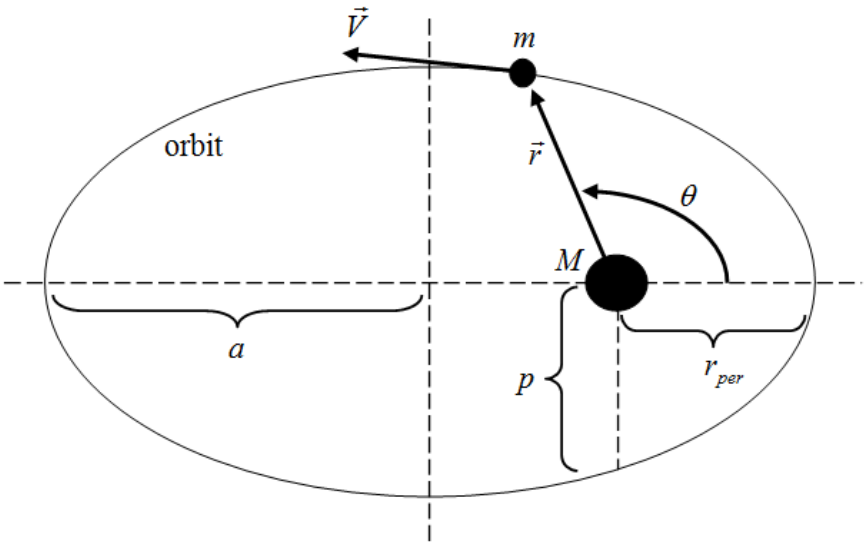

Fig. 2.1 Orbital parameters for small mass *m* in orbit about mass *M*.

Of particular interest for mission planning is the radius of periapsis r_{per}. Mission plans often specify periapsis as the point where orbit insertion burns take place, and thus r_{per} is the desired orbital radius. Alternatively, targeting r_{per} below a planet's atmosphere guarantees atmospheric entry and aids in calculation of entry parameters for a given approach. Radius of periapsis is calculated as

$$r_{per} = a(1-e) \tag{2.8}$$

Note that Eqs. (2.2-2.7) are valid for all Keplerian conic sections: circular, elliptical, parabolic, and hyperbolic orbits. The four Keplerian orbits are defined by e and ξ and are shown in Fig. 2.2.

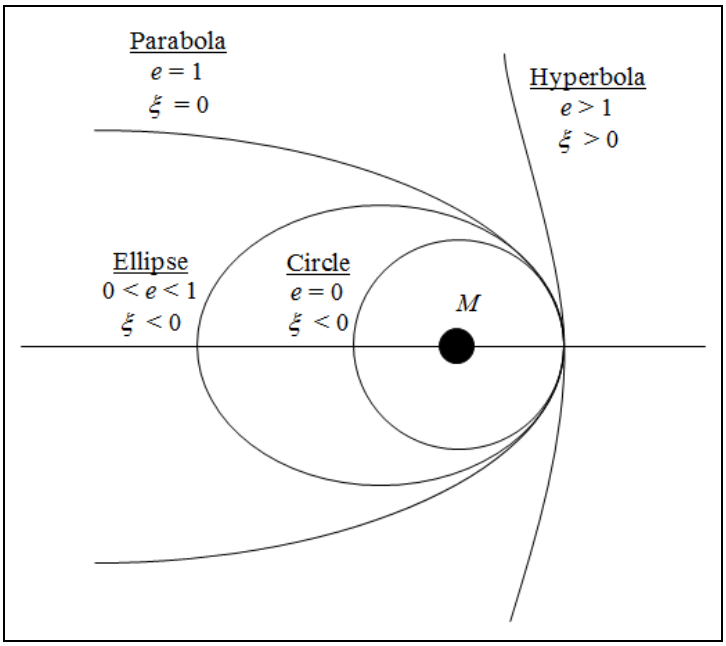

Fig. 2.2 Keplerian motion of spacecraft about a mass *M*.

2.3 Patched Conic, Zero Sphere of Influence Approximation

The method of patched conics allows for the two-body model of motion by "patching" together different conic sections. The patched conic method assumes that at any instance in time spacecraft motion is solely influenced by the gravity of a single dominant body, and the region of dominance is governed by the sphere of influence (SOI) approximation. Consider the hypothetical system given in Fig. 2.3 with a spacecraft of mass m and two large bodies with masses $M_1 > M_2$. If m is to transfer from an orbit about M_1 to a position close to M_2 it is clear that there will be a transition where the primary gravitational influence on m will switch from M_1 to M_2. Transition of influence occurs at the SOI, defined as the locus of points where the gravitational influence of M_1 and M_2 on m are equal in magnitude. In the example in Fig. 2.3, the

gravity of M_1 is the dominating influence on m everywhere except inside the SOI, where the gravity of M_2 dominates.

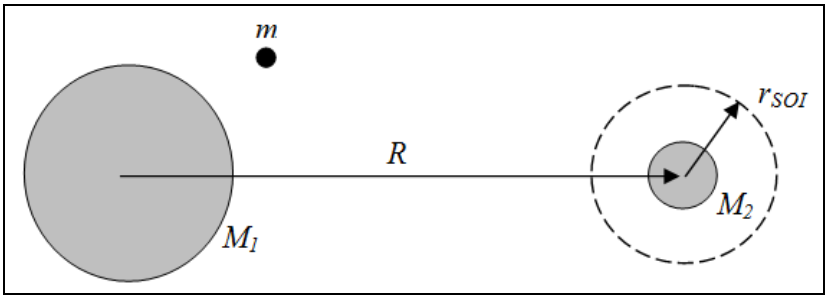

Fig. 2.3 Hypothetical system showing the SOI concept.

Transferring the SOI concept from the hypothetical system to the solar system, it is clear that the sun's gravity is the most influential gravitational force throughout most of the solar system's volume. Each planet has an SOI with approximate radius

$$r_{SOI} \cong R\left(\frac{m_{planet}}{M_{sun}}\right)^{2/5} \tag{2.9}$$

where R is the radial distance between the two bodies [3]. The r_{SOI} of the major bodies in the solar system with respect to the sun are given in Table 2.1.

Table 2.1. SOI of celestial bodies with respect to the sun [3].

Body	Mass ratio (sun-planet)	r_{SOI} (km)	r_{SOI}/R
Mercury	6.0236×10^6	1.12×10^5	0.0019
Venus	4.0852×10^5	6.16×10^5	0.0057
Earth	3.3295×10^5	9.25×10^5	0.0062
Mars	3.0987×10^6	5.77×10^5	0.0025
Jupiter	1.0474×10^3	4.88×10^7	0.063
Saturn	3.4985×10^3	5.46×10^7	0.038
Uranus	2.2869×10^4	5.18×10^7	0.018
Neptune	1.9314×10^4	8.68×10^7	0.019
Pluto	3×10^6	1.51×10^7	0.0026

Notice that the r_{SOI}/R ratio for each planet is always less than 10%. For Earth and Mars, the only two planets involved in this study, this ratio is less than 1%. Such small ratios indicate the sun's gravity is the dominating force for all but a miniscule portion of the vast distances traveled during heliocentric Earth-Mars interplanetary trajectories. The small size of the planets' regions of influence allow for use of the "zero SOI" approximation, where the planetary positions and SOI are treated as coincident points during heliocentric trajectory calculations [34].

2.4 Heliocentric Trajectories

The first step in calculating the propulsive requirements of an interplanetary transfer is determining the structure of the heliocentric transfer orbit. In the zero SOI model, the start and end locations of the transfer are readily defined as the two heliocentric planet positions $\vec{r}_{P1}(t_0)$ and $\vec{r}_{P2}(t_1)$, labeled as $\vec{r}_0(t_0)$ and $\vec{r}_1(t_1)$ in Fig. 2.4, respectively for the time of flight $TOF=t_1-t_0$. However, defining a transfer also requires knowledge of the spacecraft velocities $\vec{V}_0(t_0)$ and $\vec{V}_1(t_1)$. There is no closed-form solution for determining the orbital parameters given only two positions and a flight time, but the problem can be solved iteratively with either Kepler's problem or Lambert's problem. Lambert's problem requires three fewer design variables than Kepler's problem [31], so it is the method chosen for further discussion and implementation in optimization.

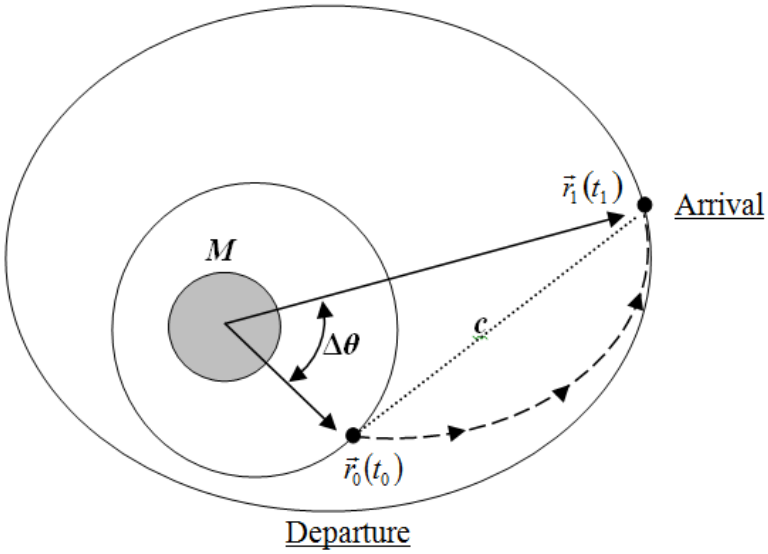

Fig. 2.4 Schematic of orbit transfer to be solved with Lambert's problem.

Lambert's theorem states that transfer time is a function of the form

$$TOF = f(r_0 + r_1, c, a) \tag{2.10}$$

where a is the semi-major axis of the transfer orbit, and c is the chord length shown in Fig. 2.4 [3]. Because methods for solving Lambert's problem are well documented a detailed algorithm is not presented here. All optimizations in this thesis use a MATLAB code written by Dario Izzo of the ESA [35]. Izzo's algorithm takes the form

$$\begin{aligned} &\text{Given:} \quad \vec{r}_0(t_0) = \vec{r}_{P1}(t_0), \vec{r}_1(t_1) = \vec{r}_{P2}(t_1), \Delta t = t_1 - t_0, \mu_M, N \\ &\text{Find:} \quad \vec{V}_0(t_0), \vec{V}_1(t_1), a, p, \Delta\theta \end{aligned} \tag{2.11}$$

where N is the number of revolutions and $\Delta\theta$ is the transfer angle. This thesis maintains $N = 0$ and $\Delta\theta \leq 180°$ throughout optimizations as $\Delta\theta > 180°$ is impractical for missions with restricted flight times, and the available simulation time prohibits exhaustive studies of tuning parameters for both conditions $\Delta\theta \leq 180°$ and $\Delta\theta > 180°$, termed type 1 and type 2 transfers, respectively. Planet positions are propagated from static ephemerides.

Higher fidelity ephemerides are available, but static ephemerides provide run-time savings and maintain a reasonable degree of accuracy for preliminary calculations [31].

The velocity of a spacecraft relative to a planet at SOI departure or arrival is $\vec{V}_\infty^+$ or $\vec{V}_\infty^-$, respectively. The "+" corresponds to departure, and "-" corresponds to arrival. These vectors are calculated with Eqs. (2.12-2.13)

$$\vec{V}_\infty^+ = \vec{V}(t_0) - \vec{V}_{P1}(t_0) \tag{2.12}$$

$$\vec{V}_\infty^- = \vec{V}(t_1) - \vec{V}_{P2}(t_1) \tag{2.13}$$

Typically, shorter transfer times require higher energies, $\vec{V}_\infty$ magnitudes, and ΔV requirements. Sections 2.5-2.6 will show that ΔV —a velocity change imparted to a spacecraft by an orbital maneuver such as orbit insertion (OI) or a trans-planetary injection burn—is often a target for minimization, as it determines the propulsive and mass requirements for a spacecraft. Section 2.5 details the calculation of ΔV requirements for the propulsive tasks of the considered round-trip Mars missions, and section 2.6 details the calculation of mass budgets from the various ΔV's.

2.5 Planetocentric Trajectories

At planetary departure or arrival, the spacecraft has velocity $\vec{V}_\infty$ relative to the planet. Note that for efficient interplanetary transfers the heliocentric $\vec{V}(t)$ typically yields $\xi < 0$, i.e. circular or elliptical orbits. Transferring $\vec{V}(t)$ from the heliocentric transfer to a planetocentric frame, however, necessarily yields energies $\xi > 0$ and a

hyperbolic section about the planet. For this reason, $\vec{V}_\infty^+$ are $\vec{V}_\infty^-$ often termed hyperbolic excess velocities.

Three planetocentric events are possible in this thesis: parking orbit departure, parking orbit insertion, or atmospheric entry. Analysis of these events is simplified by constraining motion to a plane *P* that contains the $\vec{V}_\infty$ vector and the planet center. This constraint is appropriate because no plane-change maneuvers are conducted in this thesis. It is reasonable to assume that LVs can put spacecraft in the correct orbit for planetary departure, and $\vec{V}_\infty^-$ can be placed at any point on the SOI so as to achieve the desired entry or OI conditions.

For parking orbit departure, the ΔV for the trans-planetary injection burn is calculated from the energy of the parking orbit and the energy desired at SOI exit. Using the zero SOI approximation, the energy at the SOI is calculated with Eq. (2.2) and $r=\infty$.

$$\xi_\infty^+ = \frac{V_\infty^{+2}}{2} \tag{2.14}$$

Designating the parking orbit radius as r_{per} and assuming impulsive propulsive burns, the velocity of the spacecraft at r_{per} on the departure hyperbola becomes

$$V_{per}^+ = \sqrt{2\left(\xi_\infty^+ + \frac{\mu}{r_{per}}\right)} \tag{2.15}$$

with the outgoing ΔV requirement

$$\Delta V^+ = V_{per}^+ - V_{park} \tag{2.16}$$

for a circular parking orbit velocity V_{park}. Circular speed V_{park} comes from solving Eq. (2.2) with $a = r_{per}$.

$$V_{park} = \sqrt{\frac{\mu}{r_{per}}} \tag{2.17}$$

Figure 2.5 shows the parking orbit departure for an Earth-to-Mars transfer. In this scenario, the parking orbit is LEO, and the propulsive burn conducts TMI with $\Delta V^{+} = \left\| \Delta \vec{V}_{TMI} \right\|$ from Eq. (2.16). Note that having $\vec{V}_{\infty}^{+}$ and $\vec{V}_{E}$ in the same direction maximizes the heliocentric velocity $\vec{V}(t_0)$ and energy of the spacecraft $\xi_{transfer}$ on the transfer for any imparted ΔV by utilizing the planet's significant orbital velocity. For the opposite case, orienting $\vec{V}_{\infty}^{+}$ and a planet's velocity in opposite directions minimizes ΔV requirements for transfers with $r_0(t_0) > r_1(t_1)$ by minimizing heliocentric energy for any given ΔV. Low energy transfers, the main focus in this study, with $r_0(t_0) < r_1(t_1)$ will always use orbits with $\xi_{transfer} > \xi_{P1}$ and $\xi_{transfer} < \xi_{P2}$ where ξ_P corresponds to a planet's specific energy. Low-energy transfers with $r_0(t_0) > r_1(t_1)$ likewise yield $\xi_{transfer} < \xi_{P1}$ and $\xi_{transfer} > \xi_{P2}$. These energy relations explain relative orientation of planet velocities and $\vec{V}_{\infty}$ vectors in Fig. 2.5-2.8.

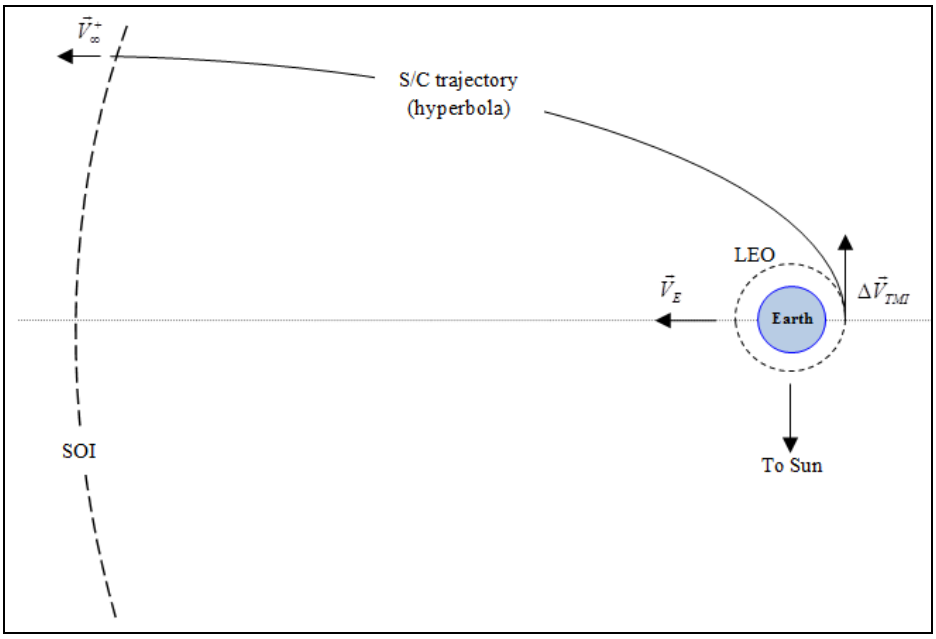

Fig. 2.5 Hyperbolic Earth departure for an Earth-to-Mars transfer.

Parking orbit insertion is a similar operation to orbit departure but with reversed chronology. Figure 2.6 shows the MOI operation with burn $\Delta\vec{V}_{MOI}$ at a low-Mars orbit (LMO) radius r_{per}. The ΔV requirement is

$$\Delta V^- = V_{per}^- - V_{park} \tag{2.18}$$

for insertion into a circular orbit at periapsis. For an MOI, $\Delta V^- = \left\|\Delta\vec{V}_{MOI}\right\|$.

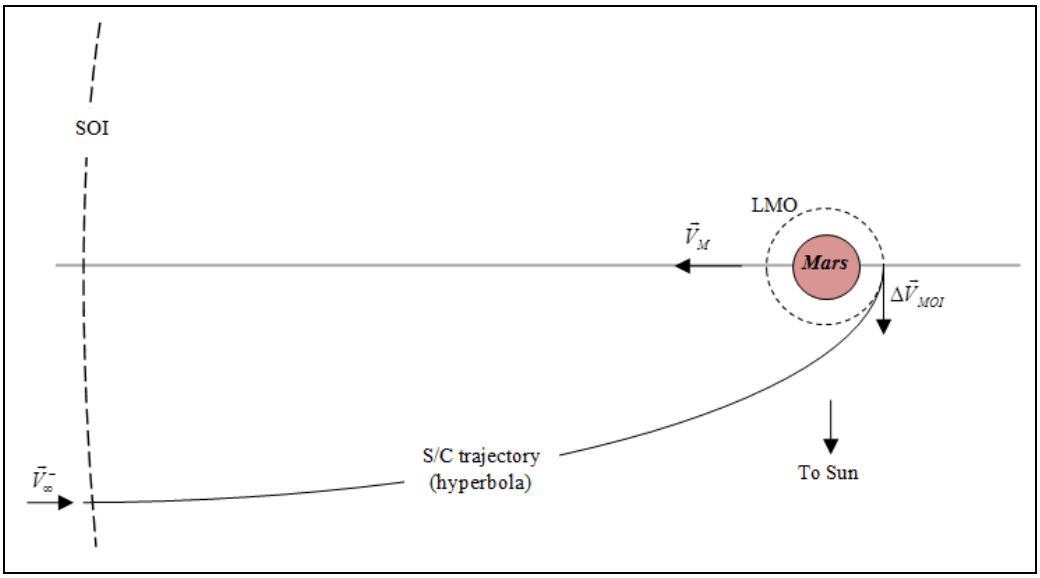

Fig. 2.6 Hyperbolic Mars arrival and orbit insertion for an Earth-to-Mars transfer.

Diagrams for low-energy Mars-to-Earth transfers are given in Fig. 2.7-2.8. Transfer departure and arrival locations are opposite from the transfer in Fig. 2.5-2.6, so the ΔV nomenclature changes to $\Delta V^+ = \left\|\Delta\vec{V}_{TEI}\right\|$ and $\Delta V^- = \left\|\Delta\vec{V}_{EOI}\right\|$ for TEI and EOI, respectively.

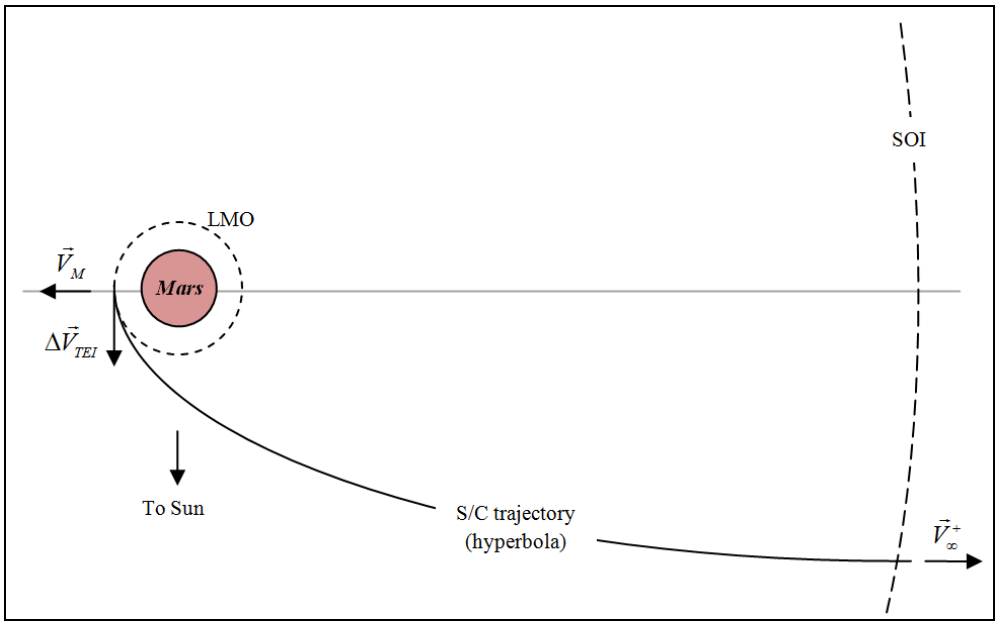

Fig. 2.7 Hyperbolic Mars departure for a Mars-to-Earth transfer.

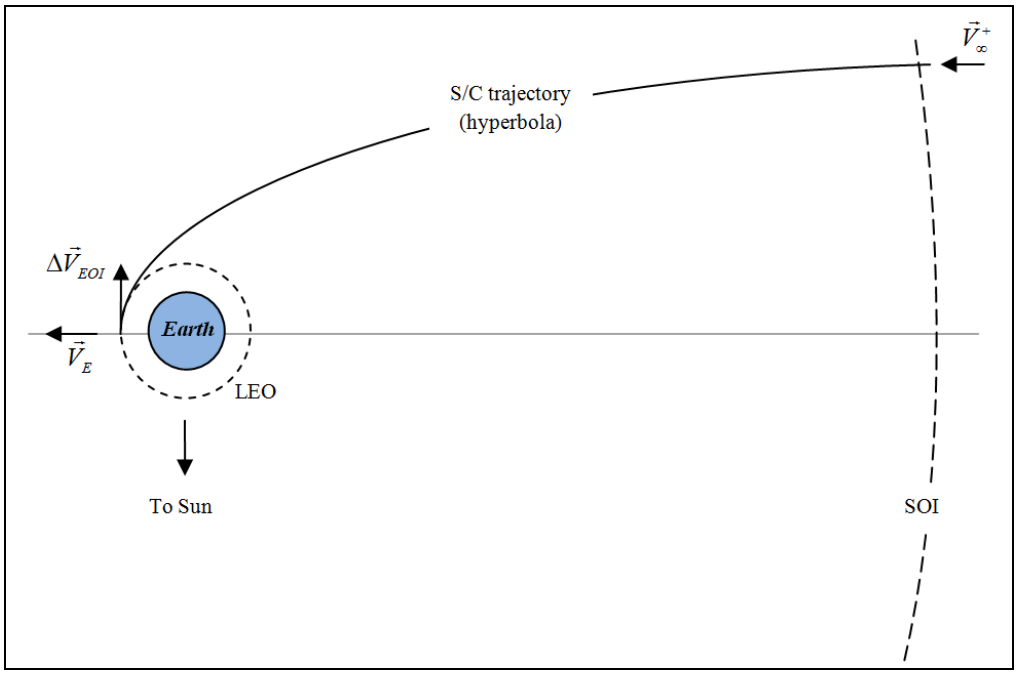

Fig. 2.8 Hyperbolic Earth arrival and orbit insertion for a Mars-to-Earth transfer..

The other possible planetocentric event is entry, descent, and landing (EDL) upon planetary arrival. Successful EDL requires meeting very strict conditions at atmospheric entry interface (EI), defined as the maximum altitude of discernible atmosphere. The velocity V_{EI} and flight-path angle γ_{EI}—the angle between the velocity vector and local horizon—at EI are two of the most important parameters. Previous successful Mars EDL schemes have used γ_{EI} ranging -11.47° to -17° (measured positive above the local horizon) and V_{EI} ranging 4.7 to 7.6 km/s [36]. Although values vary considerably between missions, error tolerances for individual missions are very tight: Slight errors in V_{EI} or γ_{EI} at r_{EI} can lead to spacecraft burn-up, atmospheric skip-out, or large errors in landing site position. The MER missions, which landed small rovers on Mars in 2004, required a 3-σ γ_{EI} error of ±0.25° [37].

Fig. 2.9 shows the scheme for direct entry at Mars. Notice that the hyperbolic approach targets r_{per} below r_{EI}. The spacecraft does not follow the hyperbolic trajectory

to r_{per} after EI, however, due to atmospheric drag. Instead, the spacecraft follows the dash-dot descent trajectory to the planet surface. Note that no illustration for Earth entry is given, because the process is identical to Fig. 2.9 if the planet title and LMO are respectively changed to Earth and LEO.

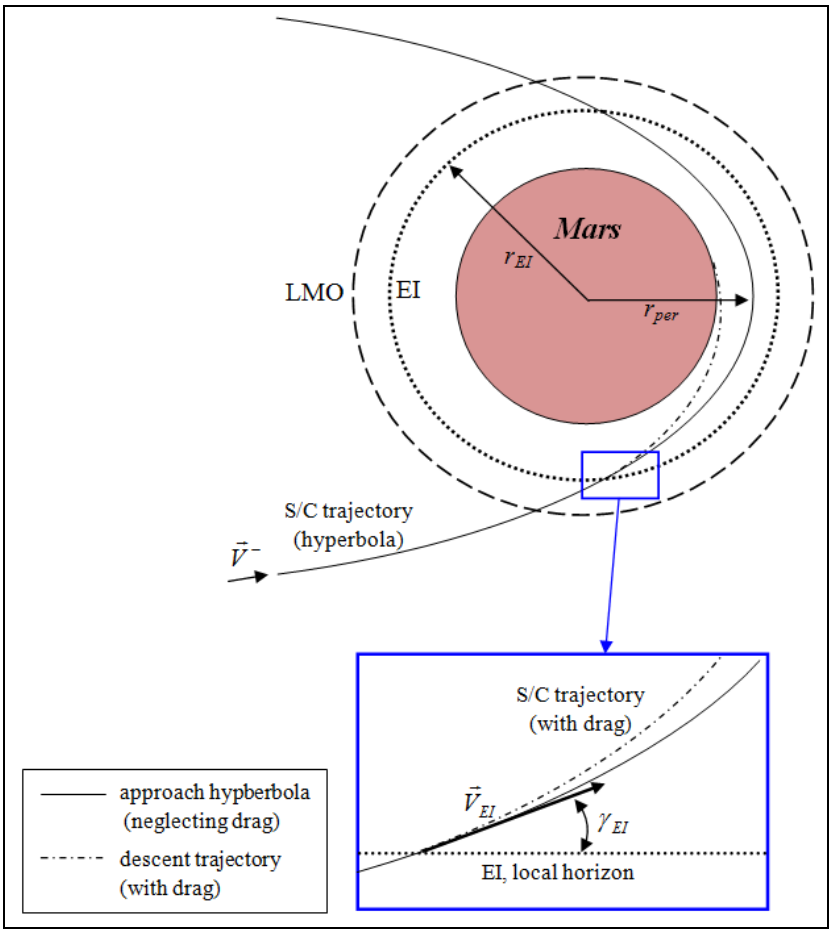

Fig. 2.9 Direct entry at Mars.

For atmospheric entry we introduce the *B*-plane which lies coincident with the planet's center, normal to $\vec{V}_\infty$, and normal to the incoming hyperbolic asymptote. Recall that $\vec{V}_\infty$ lies in plane *P*, and therefore *P* and *B* are perpendicular. The hyperbolic miss distance β, also termed the *B*-plane offset, is the distance between the hyperbolic asymptote and the planet center, shown in Fig. 2.10 with a hyperbolic planetary flyby.

With the zero SOI model, β can be given any value in the interval $(-r_{SOI}, r_{SOI})$ so as to target specific EI conditions.

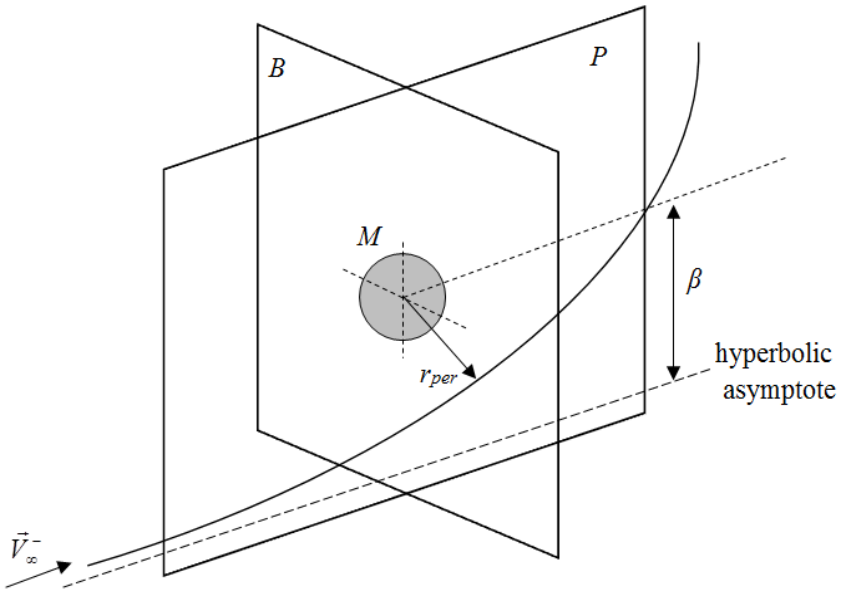

Fig. 2.10 Diagram showing *B*-plane and *P*-plane for hyperbolic flyby.

One method to target entry conditions is to designate the desired V_{EI} and γ_{EI}, then calculate the necessary *B*-plane offset to achieve that entry trajectory. Satisfactory EI targeting for this thesis is determined from energy and angular momentum equations. The energy at the SOI is calculated as in Eq. (2.14). Because energy is conserved, the velocity at r_{EI} is

$$V_{EI} = \sqrt{2\left(\xi_\infty^- + \frac{\mu}{r_{EI}}\right)} \tag{2.19}$$

from Eq. (2.2). From here, the angular momentum at EI is calculated for the specified γ_{EI}.

$$h_{EI} = r_{EI} V_{EI} \cos\gamma_{EI} \tag{2.20}$$

Finally, the hyperbolic miss distance is obtained from

$$h_{EI} = h_{SOI} = \beta V_{\infty}^{-} \tag{2.21}$$

from Eq. (2.4) for $\beta \in [0,\ r_{SOI})$. If $\beta > r_{SOI}$ the spacecraft requires a ΔV_{brake} burn to slow down just before EI. The braking burn is calculated as

$$\Delta V_{brake} = V_{EI}^{-} - V_{EI,\text{target}} \tag{2.22}$$

for target EI velocity $V_{EI,\text{target}}$, and V_{EI}^{-} is the EI velocity from the approach hyperbola calculated with Eq. (2.19). If the trajectory is designed to be unpowered, as is specified in this study, slowing burns are not permitted, $\beta > r_{SOI}$ does not yield an acceptable solution. For visualization purposes, the hyperbolic trajectory (neglecting drag) can be determined by calculating the *B*-plane offset that corresponds to a given r_{per} [3].

$$\beta = r_{per}\left[1 + \frac{2\mu}{r_{per}V_{\infty}^{2}}\right]^{1/2} \tag{2.23}$$

2.6 Mass Calculation

For the purpose of mass budget construction, a spacecraft can be divided into several different mass components: propellant m_P, tankage m_T, general spacecraft systems $m_{S/C}$, and additional structure m_S. m_S refers to structural support members, and $m_{S/C}$ includes all components that do not fit into the propellant, tank, or structural support categories. The tankage mass is directly proportional to the stored propellant mass via tankage fraction ε.

$$m_T = \varepsilon m_P \tag{2.24}$$

Similarly, m_S is proportional to the remainder of the spacecraft mass through structure fraction η.

$$m_S = \eta\left(m_{S/C} + m_P + m_T\right) \tag{2.25}$$

The total spacecraft mass before and after a propulsive maneuver, m_0 and m_f respectively, is calculated according to

$$m_0 = m_{S/C} + m_P + m_T + m_S \tag{2.26}$$

$$m_f = m_0 - m_P \tag{2.27}$$

where m_P corresponds to the propellant expended during the burn. Assuming impulsive propulsion, the ΔV achieved from the expenditure of m_P is given by the Tsiolkovsky rocket equation [34]

$$\Delta V = v_e \ln\left(\frac{m_0}{m_f}\right) \tag{2.28}$$

where v_e is the effective exhaust velocity.

$$v_e = gI_{sp} \tag{2.29}$$

Equation (2.28) is useful for calculating arbitrary propulsive burns, but it is impractical for mission planning and mass budget formulation as it requires a priori knowledge of m_0 and m_f. The impracticality comes from the fact that m_P is dependent on m_T and m_S, which are circularly dependent on m_P as seen in Eqs. (2.24-2.25). To solve this problem, Eq. (2.28) is rewritten as

$$m_0 = m_f e^{\Delta V / v_e} \tag{2.30}$$

Substituting Eqs. (2.26-2.27) then yields

$$m_{S/C} + m_P + m_T + m_S = \left(m_{S/C} + m_T + m_S\right)e^{\Delta V / v_e} \tag{2.31}$$

Further, substituting Eqs. (2.24-2.25) and rearranging for m_P gives

$$m_P = \frac{(1+\eta)\left(1-e^{\Delta V/v_e}\right)m_{S/C}}{(\varepsilon+\eta+\eta\varepsilon)e^{\Delta V/v_e}-(1+\varepsilon+\eta+\eta\varepsilon)} \tag{2.32}$$

Equation (2.32) thus gives the propellant mass required for a burn of a given ΔV and only requires a priori knowledge of $m_{S/C}$, ε, and η. General spacecraft mass $m_{S/C}$ is readily available, as it is the first quantity calculated/assumed when constructing a mass budget: It includes the fundamental science, telecommunications, and power systems required for completion of the mission goal. A structure mass fraction η=0.10 is typically used in preliminary calculations, and ε depends on the type of propellant. Solid rockets require $\varepsilon \approx 0.10$, but cryogenic propellants such as LOX and H_2 are more difficult to store and require heavier tanks with $\varepsilon \approx 0.15$ [38].

Notice that Eq. (2.32) has a singularity when the denominator equals zero. Plotting the behavior for typical NTR parameters $m_{S/C}$ = 3 MT, ε = 0.15, and I_{sp} = 900 s, Fig. 2.11 shows that the singularity is encountered when $\Delta V \approx 13.9$ km/s. m_p, from Eq. (2.27), is equal to the difference between the two curves.

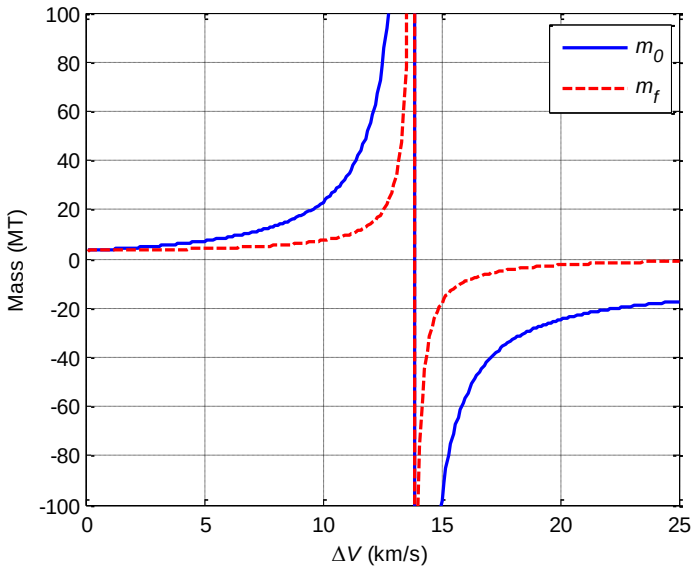

Fig. 2.11 Singularity in Eq. (2.32) with typical NTR mass parameters.

The singularity has the physical meaning that a given propulsion system has a maximum ΔV capability that is dependent on ε, η, and I_{sp}; that is, past the singularity value ΔV_{sing}, propulsion of tank and structure masses requires more propellant mass than the tank and structure can hold or support. At this point $m_P \rightarrow \infty$, and increasing V is infeasible. Note that the aforementioned guidelines for ε and η are not absolute for any system. Creative designs and advances in propellant storage may allow for lower mass fractions, thus increasing ΔV capabilities for a given spacecraft. Such capabilities are presented in Fig. 2.12-2.13, which show the performance of spacecraft with $m_{S/C}$ = 3 MT and various ε, η, and I_{sp} values.

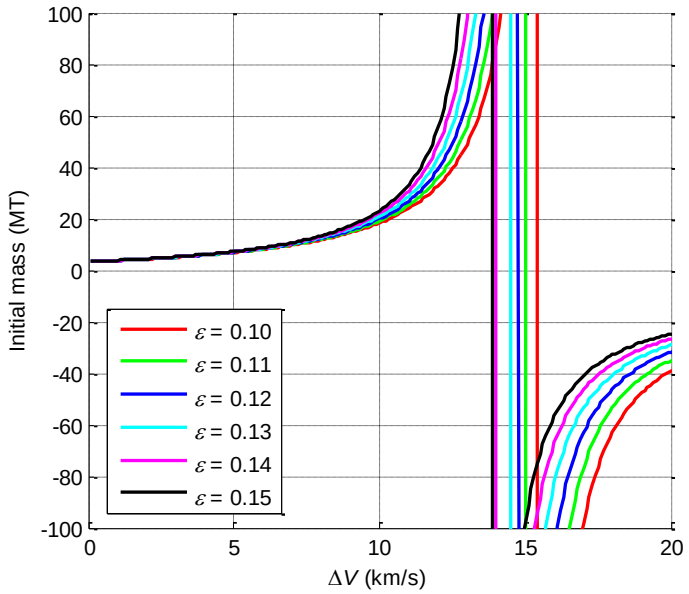

Fig. 2.12 Performance of a spacecraft with η = 0.10 and I_{sp} = 900 s for a range of ε.

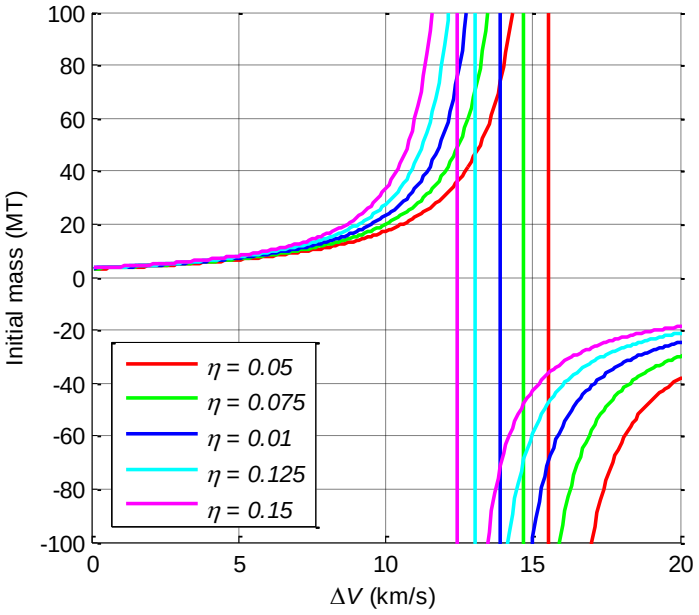

Fig. 2.13 Performance of a spacecraft with ε = 0.10 and I_{sp} = 900 s for a range of η.

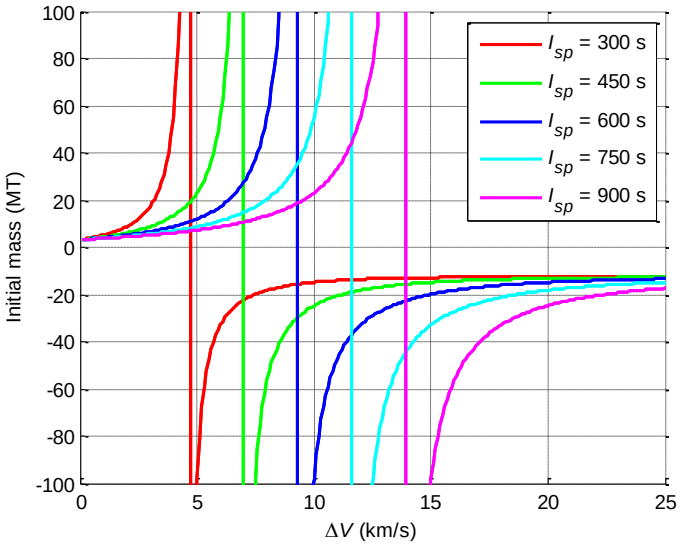

Fig. 2.14 Performance of a spacecraft with ε = 0.10 and η = 0.10 for a range of I_{sp}.

While the singularity locations are plain to see in Fig. 2.11-2.14, they are not obvious for any one set of ε, η, and I_{sp} before mapping Eq. (2.32). The unknown locations present difficulties in optimizations, as optimizing an objective function of unknown geometry allows for optimization to negative masses and infeasible transfers. Allowing calculations of negative masses is particularly troublesome for IMLEO minimizations, as solutions are driven to infeasible solutions with $\Delta V > \Delta V_{sing}$. Methods of addressing this issue are presented in section 5.2.

CHAPTER 3: MISSION ARCHITECTURE

3.1 Mars Sample Return

The mission execution timeline for a simple, single-vehicle MSR architecture can be marked by the following events listed chronologically starting with liftoff from Earth: 1) ascent from Earth's surface to LEO, 2) transfer from LEO to Mars, 3) MOI, 4) EDL at Mars, 5) ascent from Mars' surface to LMO, 6) transfer from LMO to Earth, 7) EOI, and 8) atmospheric entry at Earth. Steps 2, 3, 5, and 6 contain the major propulsive maneuvers for interplanetary transfers, whose optimization is the major focus of this thesis. These maneuvers are burns for TMI, MOI, TEI and EOI as depicted in Fig. 2.5-2.8. If direct entry is desired upon arrival at transfer destination, the OI burns are either omitted or replaced by smaller burns for slowing the spacecraft to the desired entry speed as in Eq. (2.22).

Most preliminary mission planning for ascent to LEO is satisfied by simply referencing publicly available Payload Planner's Guides (PPGs) from LV manufacturers. PPGs give accurate data for launch vehicle payload and OI capabilities. Payload and mission designers do not conduct detailed analysis of LV kinematics and trajectories; instead, launch services are contracted out to LV companies, which are tasked with delivering the payload to the desired orbit. Preliminary planning for the purpose of this thesis extends no further than addressing the launch vehicle mass and payload fairing volume constraints given by LV manufactures. Launch vehicle selection for the NTR-augmented PSDS mission is further discussed in sections 3.2-3.3.

The Earth departure leg of the mission with the TMI burn takes place as detailed in Fig. 2.5. Timeline events 1-4 and the propulsive burns for TMI and MOI are marked in Fig. 3.1 where t_0 is the time of departure from Earth, and t_1 is the time of arrival at Mars. The vectors $\vec{r}_E$ and $\vec{r}_M$ are the heliocentric positions of Earth and Mars.

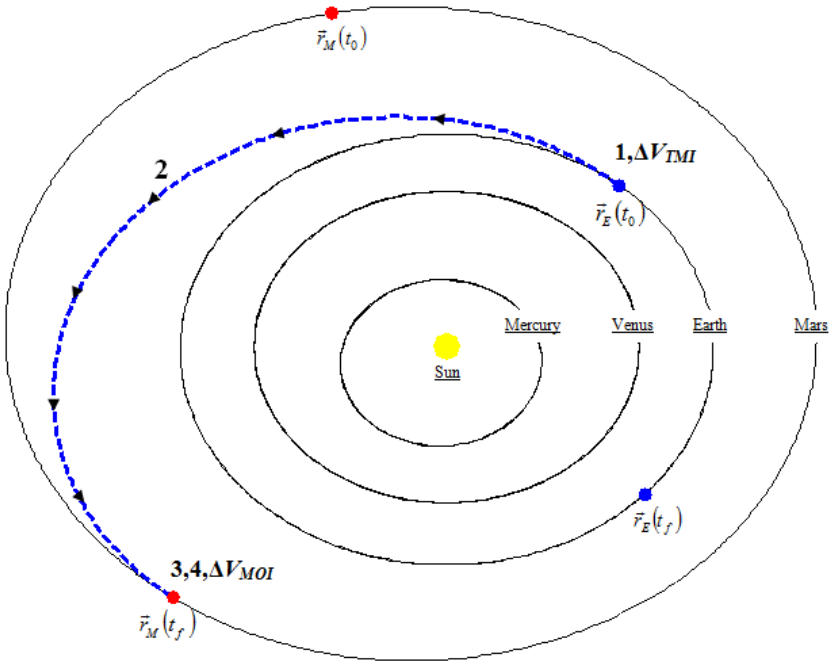

Fig. 3.1 Earth-to-Mars transfer (planet sizes not to scale).

Similar to Fig. 3.1, Fig. 3.2 shows locations timeline events 5-8 and propulsive burns for TEI and EOI.

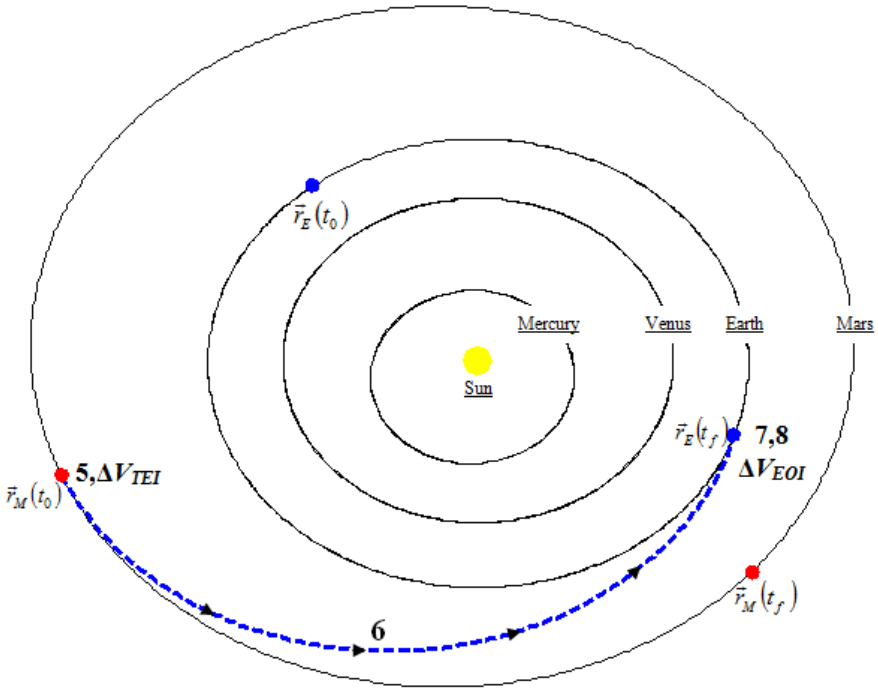

Fig. 3.2 Mars-to-Earth transfer (planet sizes not to scale).

Figures 3.1-3.2 both depict low-energy transfers. Notice that the planet, spacecraft, and hyperbolic excess velocities are nearly parallel for each planetary departure or arrival, thus making use of the planets' orbital velocities and minimizing the need for plane change maneuvers. Figure 3.3 gives the related visualization of the vectors from Eqs. (2.12-2.13).

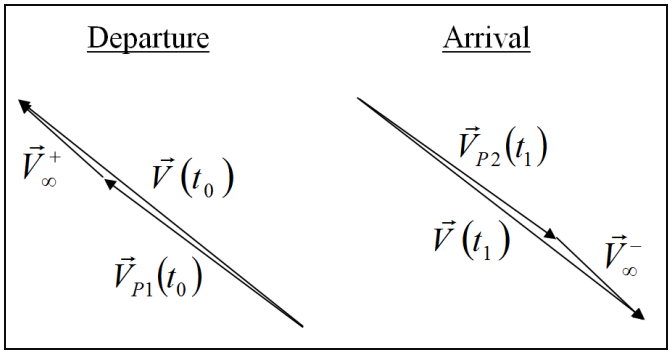

Fig. 3.3 Spacecraft, planet, and hyperbolic excess vectors for planetary departure and arrival with a low energy transfer.

Steps 1, 4, 5, and 8 are highly dependent on each mission's particular goals and physical spacecraft designs. Because this thesis limits analysis to PSDS-derived architectures, the detailed mission steps are omitted here and instead explained in sections 3.2-3.3.

3.2 2010 Planetary Science Decadal Survey

The 2010 NASA and NRC PSDS conducted a sweeping canvas of the planetary science community in order to assess, educate, and provide direction for its members. The survey aimed to determine the state of knowledge of the solar system, inventory top-level scientific questions, decide which questions should guide flight and research programs, and make research recommendations for maximizing science return. Recommendations included a prioritized list of missions in the NASA New Frontiers and larger mission classes that should be pursued in the 2013-2022 timeframe, and detailed mission architectures were constructed for high-priority missions. With approximately 30 major missions investigated, the PSDS designated MSR are the top priority mission for the next decade [18].

The MSR architecture decided upon by the PSDS is as follows. The mission is carried out by three separate spacecraft packages. The first package is launched aboard an Atlas V 531 in 2018 and contains a large science rover [20]. The rover's mission is to traverse approximately 20 km of the Martian surface over 5 years, performing science experiments and collecting samples of interest. For EDL at Mars, the rover uses the same "Sky Crane" propulsive/tethered descent system that will be used for the Mars Science Laboratory mission in 2012.

The initial PSDS plan called for two rovers—one each from NASA and ESA—but revised budget estimates resulted in a call for the construction of a single, larger rover [39]. Current plans are to build the rover in Europe and outfit it with European and American instruments. Construction will be largely based on preliminary designs for the ESA ExoMars rover, shown in Fig. 3.4.

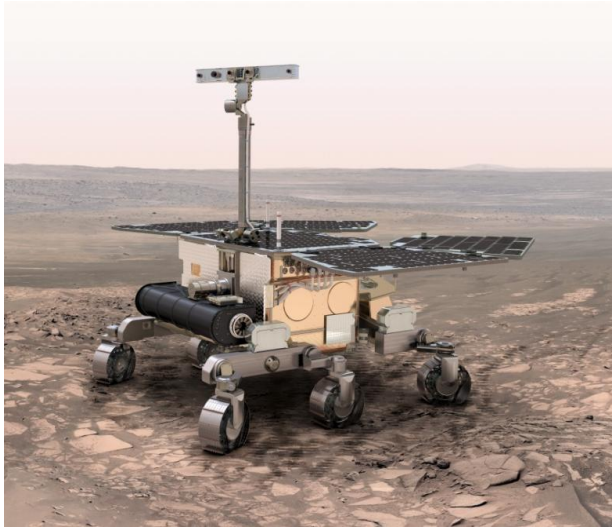

Fig. 3.4 ESA's ExoMars rover [40].

Table 3.1 gives the PSDS mass budget for the first package [20]. For analysis purposes, this study assumes that the revised rover will have a mass comparable to the sum of the two original rovers.

Table 3.1 Rover package mass budget.

Component	Mass (kg)
MAX-C rover (NASA)	364.5
ExoMars rover (ESA)	300.0
Pallet	297.4
Descent stage	802.9
Entry stage	1,550.7
Cruise stage	498.7
Total	**3,814.2**

The second package is a Mars orbiter that provides telecom for the first and third packages, carries out the TEI burn with samples aboard, and aligns the sample-containing Earth entry vehicle (EEV) on the correct entry trajectory. The spacecraft is launched into orbit and towards Mars in 2022 aboard via an Atlas V 551 [41]. Upon arrival at Mars, the craft inserts into a highly elliptical orbit and proceeds to aerobrake for 5-6 months until it achieves a 500 km circular orbit. Aerobraking is a process in which a spacecraft uses drag to decrease its energy by skimming a planet's atmosphere—this decrease in energy would otherwise need to be obtained from propulsive maneuvers, and thus aerobraking decreases ΔV and propellant requirements.

The orbiter stays in orbit about Mars for approximately two years before the third package arrives at Mars. Figure 3.5 shows the preliminary orbiter design used for analysis, and Table 3.2 gives the payload mass budget. Note that Fig. 3.5 shows two EEVs while Table 3.2 only incorporates one. This study calls for a single EEV, as the redundancy is unnecessary.

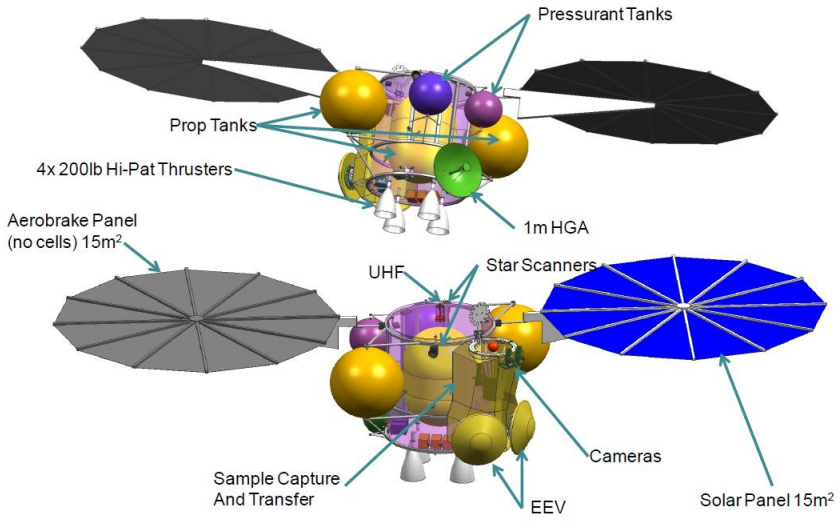

Fig. 3.5 Preliminary PSDS orbiter design [41].

Table 3.2 Orbiter mass budget.

Component	Mass (kg)
Structure/mechanisms	339.2
Propulsion (dry)	171.9
Attitude control	35.1
Power	128.4
Telecommunications	32.9
Thermal, data and command, etc.	235.4
EEV	47.2
Launch adapter	30
Propellant with contingency	2,280
Total	**3,300.1**

The third package, launched in 2024 with an Atlas V 551 [42], is a lander that contains a small fetch rover as well as a 300 kg solid rocket Mars ascent vehicle (MAV). The lander configuration and condensed mass estimate are given in Fig. 3.6 and Table 3.3, respectively.

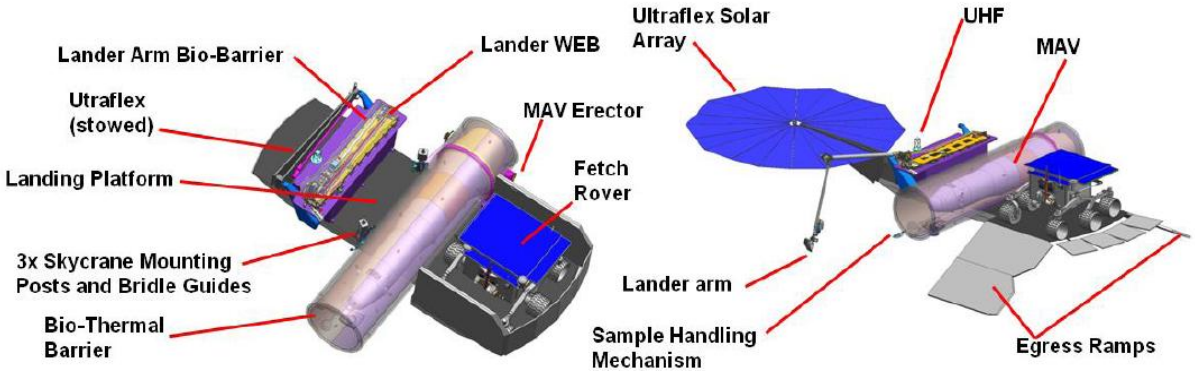

Fig. 3.6 Labeled configuration of lander platform [42].

Table 3.3 Lander package mass budget.

Component	Mass (kg)
Lander platform	553.7
Fetch rover	157.3
MAV	300
Cruise stage	573.2
Descent stage	721.5
Entry stage	1905.3
Total	**4,211.3**

The lander utilizes the same Sky Crane EDL system as the first package, entering Mars' atmosphere approximately five years after the science rover. Once the package lands, the fetch rover traverses over 12 km round-trip in six months to collect the samples from the science rover and bring them back to the MAV.

When the fetch rover completes its mission, the MAV launches into a 500-km Martian orbit and ejects the sample canister with significant separation velocity. The orbiter then rendezvous with the sample canister and secures it in the EEV. Next, the orbiter's bi-propellant propulsion system performs the TEI burn to put the spacecraft on an impact trajectory with Earth. After a 9-month transfer to Earth, it ejects the EEV on an impact trajectory for a hard landing at the Utah Test and Training Range, a site used for the previous Stardust comet sample return mission. Once the EEV is ejected, the orbiter diverts away from Earth such that it will never enter the Earth's atmosphere. The samples are finally returned to Earth in 2027.

3.3 NTR-Augmented Architecture

This study proposes an MSR mission architecture that mates the PSDS with the CSNR's affordable NTR concept to create a low-cost, near-term, and practical NTP development plan. The strategy only includes two major alterations to the original architecture: 1) All payloads are combined for Earth-to-LEO launch aboard a single SpaceX Falcon Heavy LV (as opposed to three Atlas V's), and 2) TMI is carried out with a single Pewee-derived NTR instead of the three Atlas V Centaur stages. After TMI, the NTR is discarded, and remainder of the mission is carried out as detailed in the PSDS.

The combined payload with the NTR TMI stage is shown in Fig. 3.7 in the payload fairing of a Falcon Heavy LV. The LV substitution is made possible by the volume and mass savings that come from using an NTR for TMI. The substitution also results in launch cost savings of $600 million that can then be allocated to fund the majority of the $700 million NTR development program.

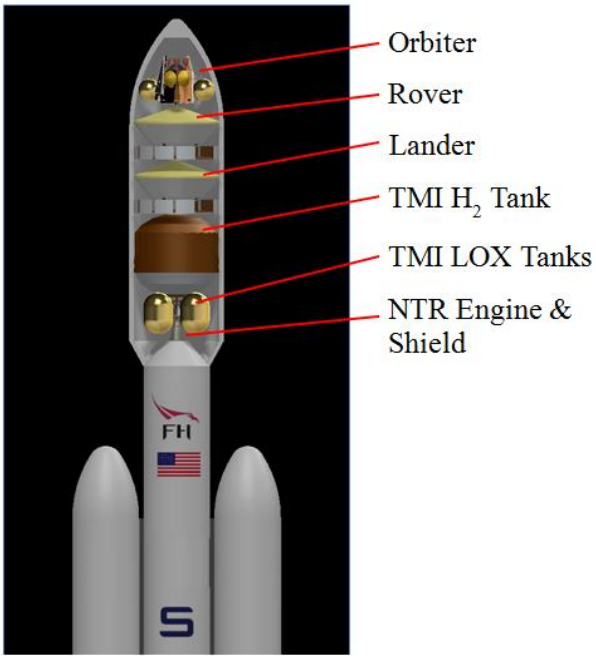

Fig. 3.7 Combined payload packages and NTR inside Falcon Heavy payload fairing.

When designing an alternative to well-received architecture, it is desirable to minimize changes to the original mission design in order to maximize acceptance with the space community. Specific to this study, it is desirable to only make changes to the original PSDS architecture that are necessary and enabling for incorporation of the Pewee-derived NTR. The proposed architecture thus uses payload package hardware identical to the PSDS except for one alteration: Cruise stages of the first and third packages are omitted. Individual cruise stages are nearly identical in structure and purpose, so this study assumes that an enlarged version of the orbiter cruise stage is sufficient to fulfill the requirements of the combined configuration. In order to conservatively estimate the mass of the enlarged system, mass budget calculations incorporate a 45% propellant contingency for all orbiter maneuvers and add the associated tank and structure masses as detailed in section 2.6. The dry mass of the configuration excluding TMI and TEI tanks and structures is given in Table 3.4.

Table 3.4 Dry mass of TMI payload with NTR and shielding.

Component	Mass (kg)
Rover package	3,315.5
Orbiter package	1,020.1
Lander package	3,638.1
Pewee-derived NTR	2,550
NTR shielding	500
Total	**11,023.7**

The V_{EI} limits for the two Mars entry craft in this study—the science rover and lander entry capsules—are derived from historical missions. To date, NASA has used Mars V_{EI} ranging 4.70-7.26 km/s, with the largest velocity corresponding to Mars Pathfinder [37]. This study's entry capsule masses and methods are similar to the 2,800 kg MSL entry capsule which plans to use V_{EI}=6 km/s; consequently, this study places the upper limit of $V_{EI,max}$=6 km/s on Mars entry craft.

The EEV V_{EI} constraint is derived from the NASA Stardust mission which used entry methods and hardware very similar to the PSDS. Stardust successfully returned a 46 kg EEV to Earth with a V_{EI} =12.9 km/s [43]—the greatest V_{EI} achieved by any mission to date. To remain conservative with the 47.2 kg PSDS EEV, this study uses an upper bound of $V_{EI,max}$=12.7 km/s.

The proposed architecture also employs a LOX-augmented NTR (LANTR). LANTRs inject oxidizer-rich gases into the H_2 flow stream in the supersonic section of the nozzle, downstream of the throat [12]. The heavier LOX increases the density of the exhaust gasses, effectively increasing thrust at the expense of I_{sp}. LANTRs are invoked by many modern NTP studies as a means to increase thrust of nominally H_2-propelled

rockets [10]. In the case of this study, however, LOX augmentation is not necessary for thrust but for volume considerations.

NTRs with pure H_2 propellant result in the lowest-mass transfers, but, for propellant masses greater than several MT, the extremely low cryogenic H_2 density of 67.2 kg/m^3 requires exorbitant tank volumes that do not fit in available LVs. To address this issue, LANTR is employed with an O_2/H_2 (oxidizer/fuel, or O/F) mass ratio O/F=4 in order to reduce tank size to the maximum volume allowed by Falcon Heavy payload fairing. Based on the calculated TRITON performance, O/F=4 yields I_{sp}=522 s and increases thrust by a factor of 3 [44]. Even with this nearly 400 s decrease in I_{sp}, the LANTR performance still exceeds the alternative chemical systems. Figure. 3.8 shows that the cryogenic O_2 density of 1,141 kg/m^3 results in significant volume savings at the expense of I_{sp}. for a range of O/F ratios.

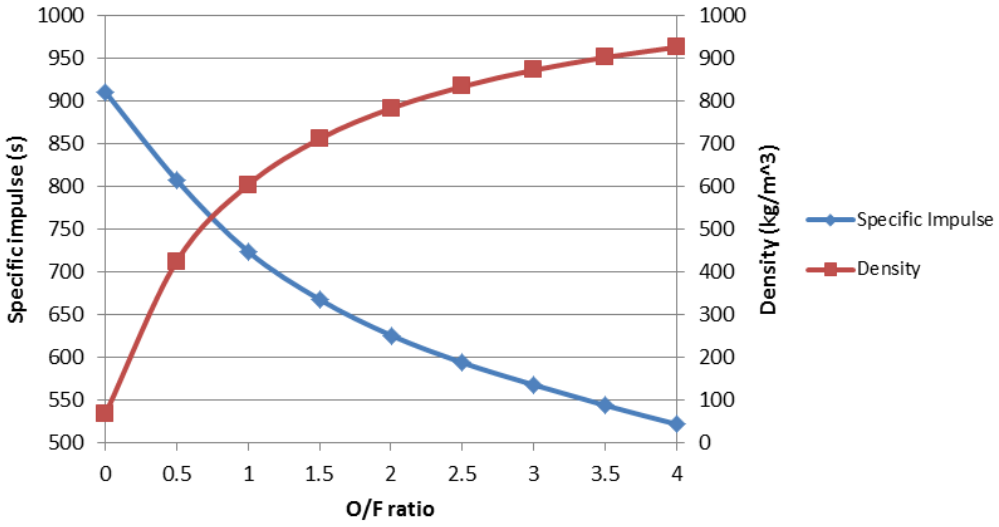

Fig. 3.8 I_{sp} and density tradeoff for LANTR for the Pratt & Whitney TRITON [44].

Table 3.5 gives the cost estimate of the affordable NTR plan as described in section 1.1.3. The budget, developed by the CSNR, includes the major program aspects that need to be addressed.

Table 3.5 Costs of NTR development activities [45].

Development activity	Cost ($M in 2015)
Fuel development and certification	85.53
Fuel costs	21.24
Engine development	238.01
Engine testing	59.59
Launch facility upgrades	11.18
LV upgrades	31.12
Security upgrades	11.72
Education/outreach programs	23.15
Project management	92.70
Reserves	137.91
Total	**712.16**

Security and launch facility upgrades come from requirements for handling and storing nuclear material on each site. LV upgrades are required for incorporating the NTR into launch ship, but incorporation should not be significantly more complicated than integrating the payload of any other mission. The given budget also allocates funds for education and outreach in order to inform the public of the technology and its associated risks.

Table 3.6 compares the cost of the PSDS and NTR-augmented PSDS architectures. Note that the NTR-augmented version costs $82 million or 1.33% more than the original plan. It is important to acknowledge that the affordability of the proposed mission relies heavily on successful test flights of the Falcon Heavy within the next several years, as the rocket has yet to be proven. There is a possibility that test

flights will be unsuccessful, consequently invalidating the launch cost savings and the cost projections of the presented plan.

Table 3.6 Costs of PSDS and NTR-augmented MSR missions, given as $M in 2015 [20,41,42,45].

Mission aspect	PSDS	NTR-augmented
Rover*	1,823.40	1,823.40
Orbiter	805.17	805.17
Lander	1,876.74	1,876.74
Mars sample return and handling	475.74	475.74
NTR development and testing	0	712.16
Launch services	775.6	149.55
Mission operations	341.5	338.02
Total	**6,099.15**	**6,180.78**

*Rover costs have changed with altered plans, but these changes do not affect absolute relative cost of the two missions

CHAPTER 4: DIFFERENTIAL EVOLUTION

Differential evolution is a stochastic, population-based direct search method that optimizes using the principles of mutation, crossover, and selection from biological evolution. DE was designed to meet four basic criteria: 1) compatibility with complex, nonlinear, non-differentiable, and multimodal cost functions, 2) parallelizability for computational efficiency, 3) ease of use with a minimal number of tuning parameters, and 4) robust convergence [24]. The algorithm's stochastic method of population variation addresses the first and second criteria, and its self-organizing nature with only three control parameters addresses the third. Multiple benchmarking studies [29,31,33] evidence robustness, even with non-optimal tuning parameters.

The three major DE tuning parameters are population size *NP*, crossover probability *CR*, and differencing weight *F*. Most studies discussed in section 1.4 use static, default tuning parameters for benchmarking trials. As is true for any routine, though, convergence can be highly dependent on tuning parameter values. Olds et al. conducted a systematic investigation of tuning parameters for trajectory optimizations and found that DE convergence for given set of tuning parameters varies between trajectory problems [31]. This thesis conducts analysis in a manner highly similar to [31] in order to facilitate comparison and conduct an exhaustive study over the entire range of possible parameter values.

It is worth mentioning that a number of studies have developed methods for self-adapting control parameters [46,47,48], but such methods are unnecessary for this study. This thesis aims to characterize DE behavior over wide ranges of tuning parameter values, not only to determine the best parameters for optimization of Mars missions but

also for the simple sake of characterization. While adaptive methods have the potential to be extremely useful for optimizations of unknown objective function geometry, implementation for this study would counteract the goal of fully exploring the design space. If the routine developed in this thesis is applied to trajectory problems of significantly different structure in the future, the author recommends implementing one of the more promising self-adaptation schemes such as those detailed in [47,48].

The first step in the DE routine is the initiation of a population of *NP* design vectors $\vec{x}_i$ for all integers $i \in [1,NP]$. Each $\vec{x}_i$ has *D* elements where *D* is the number of design variables of the optimization problem, and $\vec{x}_i(\mathrm{j})$ references the jth design variable. Price recommends $NP=10D$, but [31] shows that alternate values can improve convergence time and success. Consequently, this thesis tests a range of *NP* to determine the best values for the considered trajectory problems.

For each $\vec{x}_i$ of the first generation, elements are generated randomly from a uniform distribution over the design space defined by lower and upper bounds $\vec{x}_{lb}$ and $\vec{x}_{ub}$, respectively. After initialization, the DE algorithm carries out the mutation, crossover, and selection processes for each population member $\vec{x}_{i,G}$ for generations $G \in [1,G_{max}]$. The default algorithm in [49] and all referenced studies use a default maximum number of generations $G_{max}=1000$, so that value is maintained in this thesis to allow for valid comparison to previous studies.

Mutation is completed through random vector differencing. For each target vector $\vec{x}_{i,G}$, three random vectors $\vec{x}_{r1,G}$, $\vec{x}_{r2,G}$, and $\vec{x}_{r3,G}$ are selected from the population. The mutant vector $\vec{v}_{i,G+1}$ is then generated through the operation

$$\vec{v}_{i,G+1} = \vec{x}_{r1,G} + F\left(\vec{x}_{r2,G} - \vec{x}_{r3,G}\right) \tag{4.1}$$

where F is the mutation scale factor. If any elements of $\vec{v}_{i,G+1}$ exceed the variable bounds the operation in Eq. (4.1) is repeated until variables fall within bounds. Price originally suggested $F \in [0,2]$, but revised studies indicate that randomly varying F on [0.5,1] for each generation or difference vector, a process called "dither," can improve convergence [27,49]. In addition to testing with constant scale factor values, [31] conducted optimizations with F chosen randomly on $F \in [-1,-1]$ for each difference vector and found that the random, uniform selection method produced the best convergence. Once again building on [31] this thesis chooses F randomly from $F \in [-1,1]$ for each difference vector.

The crossover process is carried out to create a trial vector $\vec{u}_{i+1,G}$ by mixing the mutant and target vectors. Crossover is controlled by crossover frequency $CR \in [0,1]$. For each of the D elements of $\vec{x}_{i,G}$, a random number rand(j) $\in [0,1]$ is generated and compared to CR to determine whether $\vec{u}_{i+1,G}(\mathrm{j})$ takes on the value $\vec{x}_{i,G}(\mathrm{j})$ or $\vec{v}_{i,G+1}(\mathrm{j})$. Figure 4.1 gives a visualization of the crossover operation.

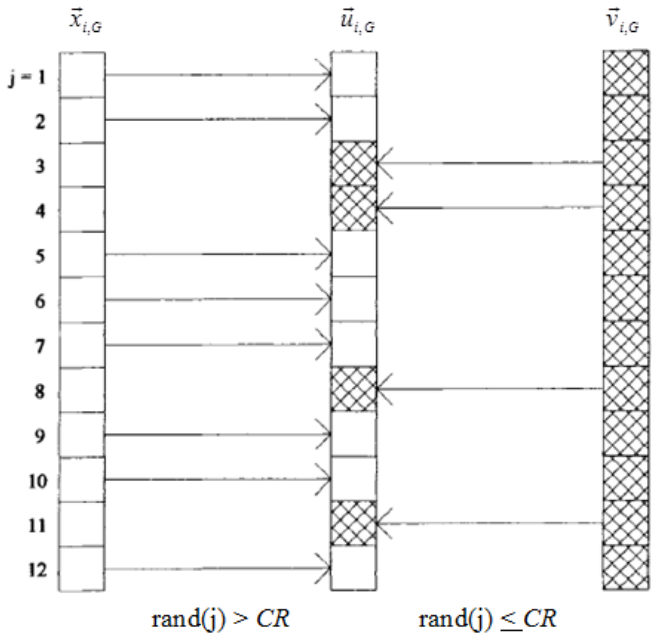

Fig. 4.1 Crossover process for formation of trial vector [31].

Next, selection is performed by evaluating the objective function f at $\vec{x}_{i,G}$ and $\vec{u}_{i,G+1}$, then choosing the better-performing vector to survive to the next generation G+1. For minimization, selection is

$$\vec{x}_{i,G+1} = \begin{cases} \vec{x}_{i,G} & \text{if } f(\vec{x}_{i,G}) \leq f(\vec{u}_{i,G+1}) \quad (4.2) \\ \vec{u}_{i,G+1} & \text{if } f(\vec{x}_{i,G}) > f(\vec{u}_{i,G+1}) \quad (4.3) \end{cases}$$

Thus, mutation and crossover effectively search the design space by altering design variables over the entirety of their possible ranges, and selection self-sorts the population by only allowing superior vectors to survive to progress to future generations.

In addition to the three primary tuning parameters, there are several ways in which DE can be altered that affect convergence. For example, G_{max} can be increased or decreased: Larger values allow for more variation and a more thorough search of the design space, but such values also require more computation time. Compared to the

effects of tuning parameters, however, variations in G_{max} have a negligible effect on convergence. The aforementioned benchmarking studies [27,29,30,31] provide evidence that G_{max} = 1000 is sufficient for convergence, so variation in G_{max} is not pursued in this study.

Another method to customize DE is to change the differencing scheme. The most common DE scheme used in previous studies [29,30,30,49], and consequently the scheme used in this thesis, is *rand/1/bin*. The first term in *rand/1/bin* indicates that vector selection is random. The second term means that only 1 vector is used for mutation, and the third time means crossover is determined by independent binary experiments. Other schemes exist such as *rand/2/bin*, using 2 vectors for mutation, and *rand/1/either-or*, using 3-point recombination instead of differential mutation [49]. Numerous studies in recent years have proposed alternate strategies for differencing and crossover, but a detailed study of those methods is beyond the scope of this thesis. The success achieved with *rand/1/bin* in [29,31] especially when compared to alternate algorithms, does not provide the motivation necessary to investigate other differencing schemes.

CHAPTER 5: OPTIMIZATION PROBLEM

5.1 Design Variables, Objective Functions, and Constraints

Optimization of the MSR trajectory requires the definition of an objective function $f(\vec{x}_i)$ that gives a measure of performance for any design variable vector $\vec{x}_i$. Because the original DE code by Storn and Price is ill-equipped to handle constraints other than lower and upper bounds on design variables, this study uses penalty methods to enforce constraints on EI velocities. In place of traditional constrained optimization methods, penalty methods use a series of unconstrained optimization problems that nominally converge to the optimum of the constrained problem. In this study, the penalty term Γ is directly proportional to constraint violations. Γ is added to the nominally unconstrained performance function f_{unc}, effectively enforcing bounds on the unconstrained routine by making undesirable constraint-violating solutions artificially costly. The objective functions take the form

$$f(\vec{x}_i) = f_{unc} + \Gamma \tag{5.1}$$

and are evaluated for each $\vec{x}_i$ tested by the DE routine.

Solving for a conic section with the Lambert problem as detailed in section 2.2 requires knowledge of departure time t_0, arrival time t_1, and radial positions $\vec{r}(t_0)$ and $\vec{r}(t_1)$. Because $\vec{r}(t_0)$ and $\vec{r}(t_1)$ are purely functions of time, the Lambert problem in this study only has two variables per transfer: t_0 and t_1. Solving the two-transfer MSR trajectory thus requires the specification of four instances in time. For the Earth-to-Mars transfer, these instances are

$$t_0 = T_0 \tag{5.2}$$

$$t_1 = T_0 + TOF_1 \tag{5.3}$$

with Earth-departure Julian date T_0 and Earth-to-Mars time of flight TOF_1. Similarly, for the Mars-to-Earth transfer

$$t_0 = T_0 + TOF_1 + T_{stay} \tag{5.4}$$

$$t_1 = T_0 + TOF_1 + T_{stay} + TOF_2 \tag{5.5}$$

with stay time at Mars T_{stay} and Mars-to-Earth time of flight TOF_2. Thus, the design variable vector for optimization is

$$\vec{x}_i = \begin{Bmatrix} T_0 \\ TOF_1 \\ T_{stay} \\ TOF_2 \end{Bmatrix} \tag{5.6}$$

With the goal of minimizing IMLEO, the objective function *f* can take one of two forms depending on the restrictions placed on design space. The first, simple form stems from the behavior of Eq. (2.30): It is plain to see that minimizing ΔV also minimizes m_0. It then follows that the absolute minimum IMLEO for a two-transfer mission is obtained by solely using minimum ΔV burns. This nullifies the need for mass calculations during optimization, and the objective function takes the form

$$f(\vec{x}_i) = \sum_{j=1}^{n} \left\| \Delta \vec{V}_j \right\| + \Gamma \tag{5.7}$$

to minimize total ΔV for *n* transfers.

The second form of the objective function

$$f(\vec{x}_i) = \text{IMLEO} + \Gamma \tag{5.8}$$

is used to optimize IMLEO directly. This form is necessary because minimum ΔV burns are not always practical. Manned mission architectures typically specify non-minimum-ΔV transfers in order to achiever faster transfers that limit crew radiation exposure and time spent in zero gravity. The DRA 5.0 for example, constrains TOF_1 and TOF_2 to less than 180 days, which prohibits global minimum energy transfers [9].

For trajectories with constrained flight times, the minimum total ΔV solution often contains individual ΔV's that are greater than their global optima. Acknowledging that some maneuvers have greater influence on IMLEO than others—the propellant requirements of each burn are partially determined by the propellant requirements of all future burns—it can be seen IMLEO can be reduced from the minimum ΔV solution by decreasing the more influential ΔV's at the expense of the less important ΔV's. For illustration purposes, consider the MSR mission from section 3.3 with transfer times constrained to 180 days. Figure 5.1 shows the round-trip minimum ΔV and IMLEO solutions for a range of T_{stay} and freely varying T_0.

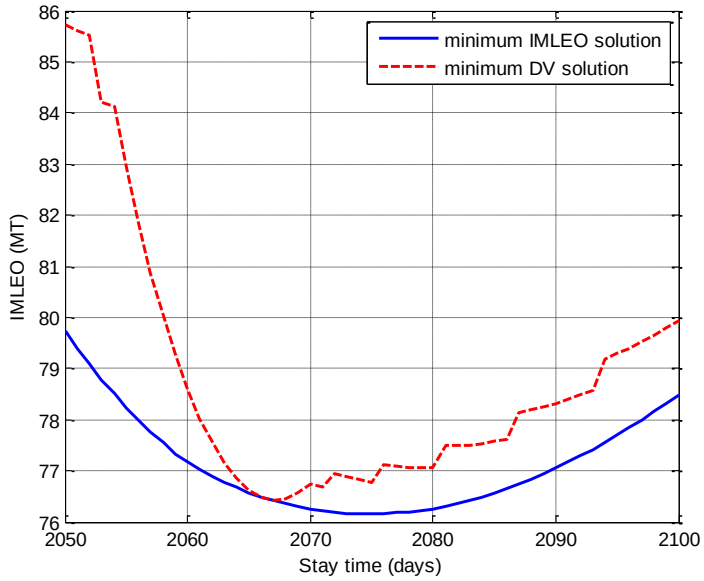

Fig. 5.1 Minimum ΔV and IMLEO solutions for a range of T_{stay} with free variable T_0 and fixed variables $TOF_1 = TOF_2$ = 180 days.

Notice that the global minima of the two solutions do not correspond. This is because, relative to the minimum total ΔV solution, the minimum IMLEO solution has a slightly lower ΔV_{TMI} but larger ΔV_{TEI}. The lower IMLEO is achieved because the propellant mass saved from slight ΔV_{TMI} reduction is greater than the propellant mass gained from the larger increase in ΔV_{TEI}.

The only constraints imposed in this study are upper bounds on EI velocities as detailed in section 2.6. While the trajectory algorithm includes Eq. (2.22) to calculate burns that slow fast-moving entry capsules to the correct V_{EI}, it is desirable to optimize to trajectories that do not require braking burns: Eliminating braking burns eliminates the need for the large propulsive systems that perform those maneuvers, thus lowering spacecraft mass. Here, penalty methods are employed to guide solutions away from trajectories that require braking burns. Note that for missions with greatly reduced flight

times, the required high velocity transfers can make omitting braking burns impractical or completely infeasible.

With penalty methods, it is possible for optimizations to converge on constraint-violating solutions, because solutions that only slightly violate constraints have miniscule penalty magnitudes. To guide the optimization away from such solutions, this study assesses penalties when $V_{EI} \geq V_{EI,max}$-0.1 km/s. Here, the imposed V_{EI} limits are $V_{EI,Earth,lim}$=12.6 km/s and $V_{EI,Mars,lim}$=5.9 km/s at Earth and Mars, respectively. The total EI penalty Γ_{EI} is calculated as

$$\Gamma_{EI} = \Gamma_{Earth} + \Gamma_{Mars} \tag{5.9}$$

where

$$\Gamma_{Earth} = \begin{cases} 0 & \text{if } V_{EI,Earth} \leq V_{EI,Earth,\lim} \\ C_{pen}\left(V_{EI,Earth} - V_{EI,Earth,\lim}\right) & \text{if } V_{EI,Earth} \geq V_{EI,Earth,\lim} \end{cases} \tag{5.10}$$

$$\Gamma_{Mars} = \begin{cases} 0 & \text{if } V_{EI,Mars} \leq V_{EI,Mars,\lim} \\ C_{pen}\left(V_{EI,Mars} - V_{EI,Mars,\lim}\right) & \text{if } V_{EI,Mars} \geq V_{EI,Mars,\lim} \end{cases} \tag{5.11}$$

with penalty constant C_{pen}.

In addition to Γ_{EI}, penalties are assessed for infeasible, negative-mass maneuvers, as detailed in section 2.6, according to

$$\Gamma_{\Delta V,\lim} = \sum_{i}^{4} \Gamma_{\Delta V,i} \tag{5.12}$$

for each propulsive maneuver *i*. The penalty for each maneuver is

$$\Gamma_{\Delta V,i} = \begin{cases} 0 & \text{if } m_p\left(\Delta V_i\right) \geq 0 \\ C_{pen}\left(\Delta V_i\right) & \text{if } m_p\left(\Delta V_i\right) < 0 \end{cases} \tag{5.13}$$

where propellant mass m_p is calculated according to Eq. (2.32). Assessing penalties in this manner makes the infeasible region artificially costly and thus drives the

optimization to the feasible region. Adding the two types of penalty terms together, the total penalty term is

$$\Gamma = \Gamma_{EI} + \Gamma_{\Delta V,\lim} \tag{5.14}$$

Penalty constants can have any magnitude, and their values greatly affect convergence of gradient-based optimization. However, DE's selection process makes convergence for this study relatively independent of the way C_{pen} shapes the objective function so long as the feasible, constraint-satisfying region of solutions is found. Finding the feasible region is not typically difficult for DE, as upwards of 10,000 different $\vec{x}_i$ are evaluated for a single run with 1000-generations. Due to DE's independence from C_{pen}, this study uses $C_{pen}=10^6$ for both objective functions and Eqs. (5.10-5.11) and Eq. (5.13). Although fine tuning of C_{pen} could certainly improve algorithm performance, chapter 6 will shown that the given strategy is capable of producing satisfactory convergence.

5.2 Computer Implementation

The given Mars Mission Trajectory Optimization Program (MMTOP) is implemented through a series of MATLAB m-files. The general procedure is given in Fig. 5.2. The flowchart shows the order of operations from left to right, then top to bottom. All sub-operations to the right of a box are completed before moving to the next box down; e.g. "Problem setup" and "Variable bounds" operations are completed under "Input" before moving on to "Optimization."

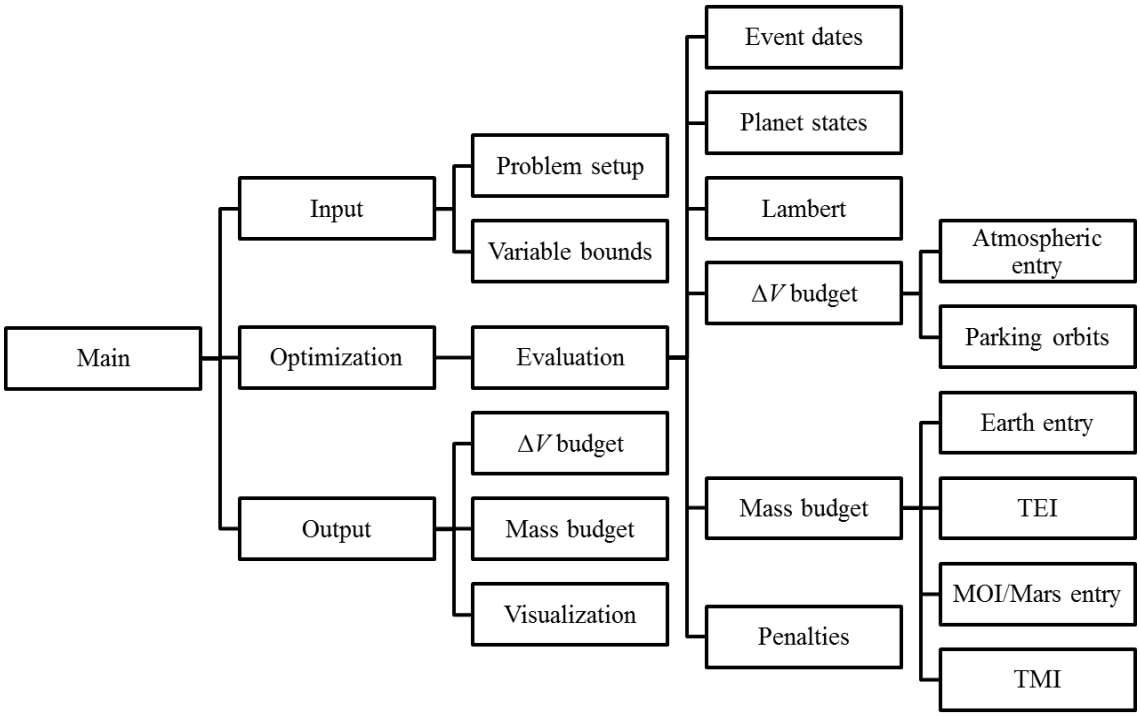

Fig. 5.2 Functional organization of the presented trajectory optimization routine.

When the main program begins, "Main" calls "Input." The Input operations consist of establishing the DE parameters and defining $\vec{x}_{lb}$ and $\vec{x}_{ub}$. Next, "Main" calls the "Optimization" subroutine which contains the core DE algorithm that performs the population generation, mutation, crossover, and selection operations. For each generation *G*, "Optimization" calls the "Evaluation" subroutine for the *NP* number of design vectors $\vec{x}_i$ and evaluates the fitness of $\vec{x}_i$ with an objective function in the form of Eq. (5.7) or Eq. (5.8).

"Evaluation" first calculates the event dates through Eqs. (5.2-5.5). Next, the planet states are calculated from static ephemerides. Planet states are then given as inputs, along with TOF_1 and TOF_2, to "Lambert" which solves for transfer velocity parameters. The "ΔV budget" subroutine computes ΔV requirements of each mission leg with the relations given in section 2.5. If the objective function is Eq. (5.8), the

"Mass budget" subroutine calculates the mass requirements for each leg of the mission via Eq. (2.32) and the specified spacecraft masses from sections 3.2-3.3. Mass calculations are carried out in reverse chronological order of the mission timeline, as the propellant requirements of each maneuver are dependent on the tank, propellant, and structure masses associated of all subsequent maneuvers.

The "Penalties" subroutine assesses penalties based EI requirements as detailed in section 5.1. Velocity parameters of high energy trajectories can be so great that no feasible transfer exists that yields $V_{EI} \geq V_{EI,\max}$ unless a braking burn is employed. In this case the algorithm will still run, but the objective function geometry will be distorted such that it no longer accurately depicts the ΔV or IMLEO requirements of any given $\vec{x}_i$.

Once the maximum number of generations is reached, "Optimization" passes the best $\vec{x}_i$ to "Output." The "Output" subroutine then calculates ΔV and mass budgets for the mission, and it produces a video or static plot of each interplanetary transfer. The mass budget includes $m_{S/C}, m_P, m_T,$ and m_S for each propulsive maneuver as well as m_0 and m_f for each leg of the mission. The ΔV budget includes each ΔV for trans-planetary injection, OI, and braking burn as well as V_{EI} values that indicate the success of matching EI conditions.

CHAPTER 6: RESULTS

6.1 Benchmarking

Before MMTOP can be applied to the MSR mission from chapter 3, MMTOP effectiveness must first be benchmarked by comparing the physical model and optimization routine with results of published literature. Of the trajectory studies referenced thus far, [26]—which uses the Jet Propulsion Laboratory (JPL) QUICK mission analysis software—is the most appropriate for comparison due to similarities in mission design. Table 6.1 presents optimization results from [26] and MMTOP for several mission variations. The bounds used for MMTOP trials are $\vec{x}_{lb} = \vec{x}_{QUICK} - 200$ and $\vec{x}_{ub} = \vec{x}_{QUICK} + 200$ where $\vec{x}_{QUICK}$ is the optimum solution from the JPL software. Because [26] optimizes for C_3 only, the MMTOP objective function is set to match: optimizing for C_3 is very similar to Eq. (5.7) without the penalty term and the OI burns.

Table 6.1 Comparison of QUICK and MMTOP results for selected architectures.

Mission variation	Parameter	QUICK	MMTOP
1	T_0 (month, day, year)	[9 23 2007]	[9 23 2007]
	TOF_1 (days)	209	210
	T_{stay} (days)	490	486
	TOF_2 (days)	261	263
	Earth-to-Mars $\boldsymbol{C_3}$ (km^2/s^2)	18.8	18.8
	Mars arrival $\boldsymbol{V_\infty^-}$ (km/s)	3.9	3.9
	Mars-to-Earth $\boldsymbol{C_3}$ (km^2/s^2)	9.4	12.3
	Earth arrival $\boldsymbol{V_\infty^-}$ (km/s)	3.2	3.4
2	T_0 (month, day, year)	[12 27 2013]	[12 27 2013]
	TOF_1 (days)	208	208
	T_{stay} (days)	495	495
	TOF_2 (days)	237	237
	Earth-to-Mars $\boldsymbol{C_3}$ (km^2/s^2)	9	9
	Mars arrival $\boldsymbol{V_\infty^-}$ (km/s)	5.3	5.4
	Mars-to-Earth $\boldsymbol{C_3}$ (km^2/s^2)	5.6	5.7
	Earth arrival $\boldsymbol{V_\infty^-}$ (km/s)	5.2	5.3
3	T_0 (month, day, year)	[5 17 2018]	[5 17 2018]
	TOF_1 (days)	235	235
	T_{stay} (days)	516	516
	TOF_2 (days)	191	191
	Earth-to-Mars $\boldsymbol{C_3}$ (km^2/s^2)	7.7	7.7
	Mars arrival $\boldsymbol{V_\infty^-}$ (km/s)	3.3	3.3
	Mars-to-Earth $\boldsymbol{C_3}$ (km^2/s^2)	11.4	11.5
	Earth arrival $\boldsymbol{V_\infty^-}$ (km/s)	3.3	3.3

Table 6.1 shows that the optimized $\vec{x}_{QUICK}$ and $\vec{x}_{MMTOP}$ are very similar for each mission option. Time variables never differ by more than four days, and C_3 and V_∞^- values are nearly identical except for the return leg in the first mission variable. The

closeness of the solutions shows that MMTOP produces results highly similar to industry software and is therefore acceptable for use with new mission architectures and timelines.

6.2 MSR Design Space, Optima, and Model Verification

MMTOP optimizations for ΔV and IMLEO are carried out for every combination of the four population sizes *NP*: 10, 20, 30, and 40 and the five crossover probabilities *CR*: 0.2, 0.4, 0.6, 0.8, and 1. Each combination is tested on several different design spaces in order to test algorithm effectiveness with different mission structures. The different design spaces considered are given in Table 6.2.

Table 6.2 Optimization scenarios.

		Design variable bounds			
Case	**Obj. function**	T_0 **(year)***	TOF_1 **(days)**	T_{stay} **(days)**	TOF_2 **(days)**
A	ΔV	[2026 2052]	[60 1095]	[1400 2500]	[60 1095]
B	IMLEO	[2020 2052]	[60 1095]	[1400 2500]	[60 1095]
C	ΔV	[2026 2029]	[60 1095]	[1400 2500]	[60 1095]
D	IMLEO	[2026 2029]	[60 1095]	[1400 2500]	[60 1095]
E	ΔV	[2026 2029]	[60 180]	[1400 2500]	[60 180]
F	IMLEO	[2026 2029]	[60 180]	[1400 2500]	[60 180]
G	ΔV	$[T_{0,opt} \pm 5]$**	$[TOF_{1,opt} \pm 5]$	$[T_{stay,opt} \pm 5]$	$[TOF_{2,opt} \pm 5]$
H	IMLEO	$[T_{0,opt} \pm 5]$**	$[TOF_{1,opt} \pm 5]$	$[T_{stay,opt} \pm 5]$	$[TOF_{2,opt} \pm 5]$

*The lower bound is Jan. 1st of the first year, and the upper bound is Dec. 31st of the second year.
**Units in days. All bounds for these trials are $\vec{x}_{opt} \pm 5$ days where $\vec{x}_{opt}$ is the optimum for cases A-D (minimum energy transfers).

The bounds on cases A-D and G-H allow for optimization to global minimum ΔV transfers, whereas cases E-F restrict the solution space to non-global minima. Cases

A-B test over a 32-year timespan which contains two 15-year synodic periods. Cases C-F test over a 3-year timespan that contains the global optimum of the 32-year window—Fig. 6.1 shows the approximate optima for missions with unconstrained flight times in each 2.1-year period in 2020-2050.

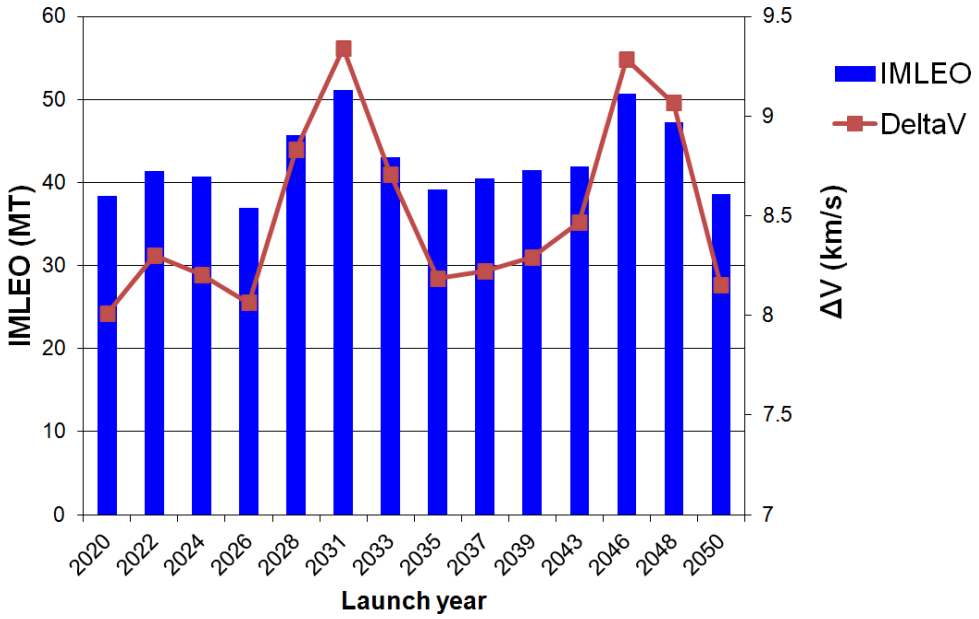

Fig. 6.1 Approximate optima for unconstrained-TOF missions in each 2.1-year synodic period within the 2020-2050 timeframe.

Cases G-H bound each design variable to ± 5 days from the optimum value from cases A-D: the idea here is to use the results of one of the trials with large design spaces, i.e. cases A-D, to define bounds for cases G-H.

In addition to judging success as convergence on the best-known minimum ΔV or IMLEO, results are presented based on each solution's proximity to the optimum $\vec{x}_{opt}$. The three success criteria are detailed in Table 6.3.

Table 6.3 Success criteria definitions.

Designation	Criteria
D1	$\Delta V_{run} - \Delta V_{opt} \leq 1\,\text{m/s}$
D2	$\text{IMLEO}_{run} - \text{IMLEO}_{opt} \leq 1\,\text{kg}$
D3	$\sum_{i=1}^{4} \left\| \vec{x}_{run}(i) - \vec{x}_{opt}(i) \right\| \leq 5\,\text{days}$

Criterion D3 measures algorithm's ability to locate the general location of the optimal solution. Knowledge of D3 performance is extremely useful: If an optimization trial over a large design space results in an $\vec{x}_{trial}$ only a limited distance from $\vec{x}_{opt}$, then $\vec{x}_{trial}$ can be used to define a reduced design space with $\vec{x}_{lb} = \vec{x}_{opt} - 5$ and $\vec{x}_{ub} = \vec{x}_{opt} + 5$ for a second optimization. Because DE depends on random numbers to generate and vary its population, reducing the design space greatly increases the probability of creating a trial vector $\vec{u}_i = \vec{x}_{opt}$, i.e. successfully optimizing D1 and D2.

The $\vec{x}_{opt}$ for each optimization scenario in Table 6.2 is given in Table 6.4, and detailed ΔV budgets are given in Table 6.5. Notice that the global optimum launch opportunity for the [2020 2052] window is in 2026, and thus $\vec{x}_{opt}$ is identical for cases A-D and G-H. Also note that for the constrained cases E-F, the optimum IMLEO solution has a greater total ΔV than the optimum ΔV solution.

Table 6.4 Optimum design variable configurations for design spaces in Table 6.2.

Performance measures			Design variables			
Case	**ΔV (km/s)**	**IMLEO (kg)**	**T_0 (mo., day, year)**	**TOF_1 (days)**	**T_{stay} (days)**	**TOF_2 (days)**
A	7.857	36,926	[11 11 2026]	271.6	1,998.2	217.4
B	7.857	36,926	[11 11 2026]	271.6	1,998.2	217.4
C	7.857	36,926	[11 11 2026]	271.6	1,998.2	217.4
D	7.857	36,926	[11 11 2026]	271.6	1,998.2	217.4
E	10.453	77,060	[12 13 2026]	180.0	2,079.7	180.0
F	10.493	76,148	[12 18 2026]	180.0	2,074.7	180.0
G	7.857	36,926	[11 11 2026]	271.6	1,998.2	217.4
H	7.857	36,926	[11 11 2026]	271.6	1,998.2	217.4

Table 6.5 ΔV budget for the optimum mission in each design space.

Case	**A-D & G-H**	**E**	**F**
C_3 (km^2/s^2)	10.502	30.947	37.254
ΔV_{TMI} (km/s)	3.660	4.527	4.783
ΔV_{MOI} (km/s)	2.212	3.813	3.598
ΔV_{TEI} (km/s)	1.985	2.113	2.113
ΔV_{EOI} (km/s)	0	0	0
Total ΔV (km/s)	7.857	10.453	10.493

Recall that due to the time required to perform an exhaustive examination of tuning parameters and the impracticality of type 2 transfers with cases E-F, this thesis limits trajectories to type 1 transfers. For cases A-D and G-H, it is likely that type 2 transfers would yield lower ΔV requirements [24,26].

The optimum trajectories for cases A-D and G-H are plotted in Figs. 6.2-6.3, and the optimum trajectories for case E are given in Figs. 6.4-6.5. Plots for case F optima are not given, as they are visually indistinguishable from Figs. 6.4-6.5.

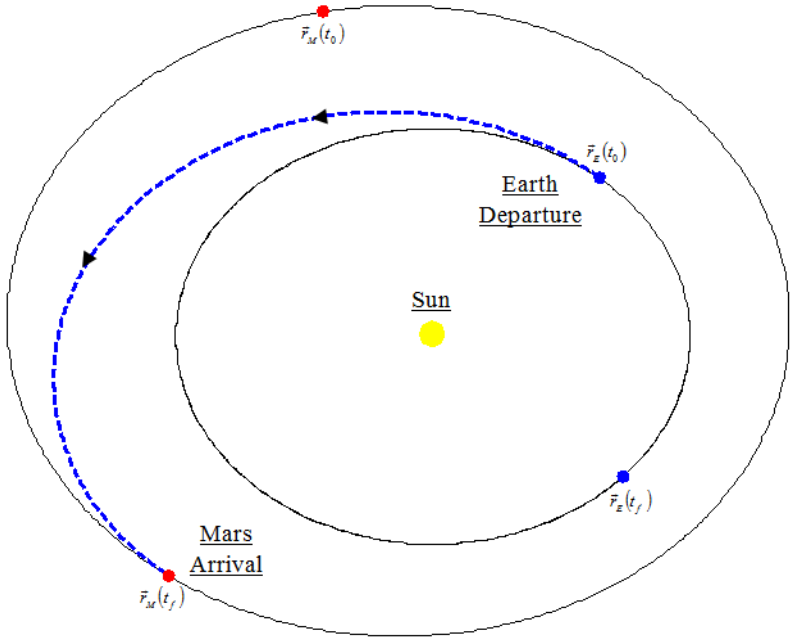

Fig. 6.2 Optimum Earth-to-Mars transfer for Cases A-D and G-H.

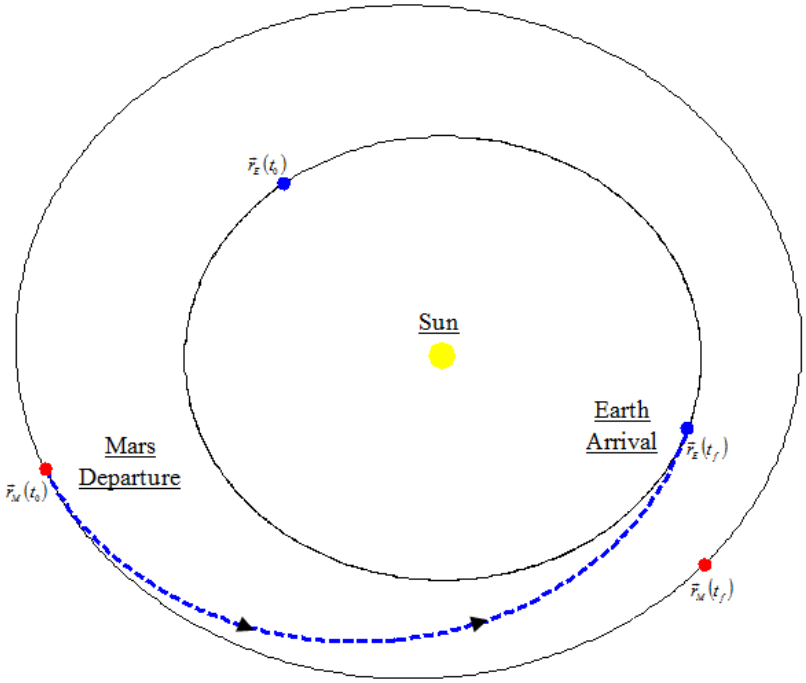

Fig. 6.3 Optimum Mars-to-Earth transfer for Cases A-D and G-H.

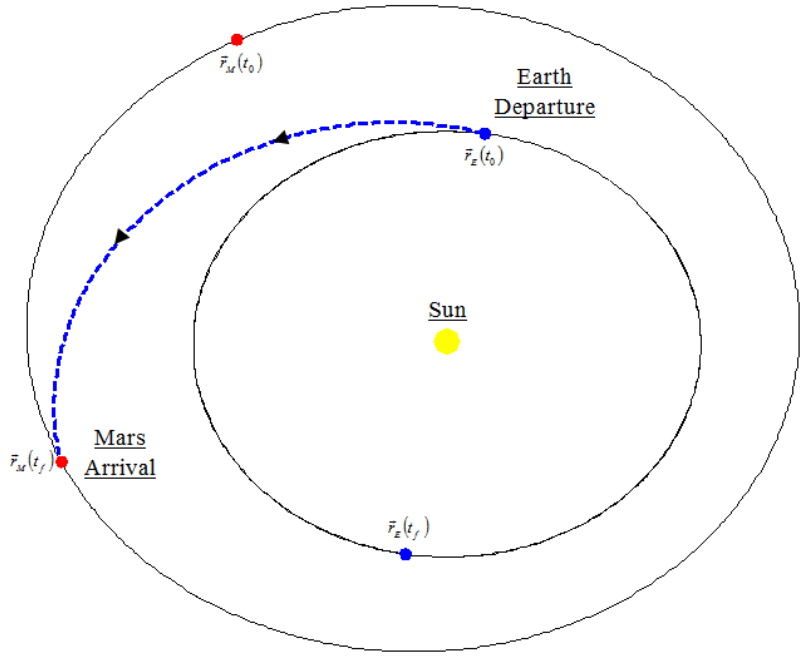

Fig. 6.4 Optimum Earth-to-Mars transfer for Case E.

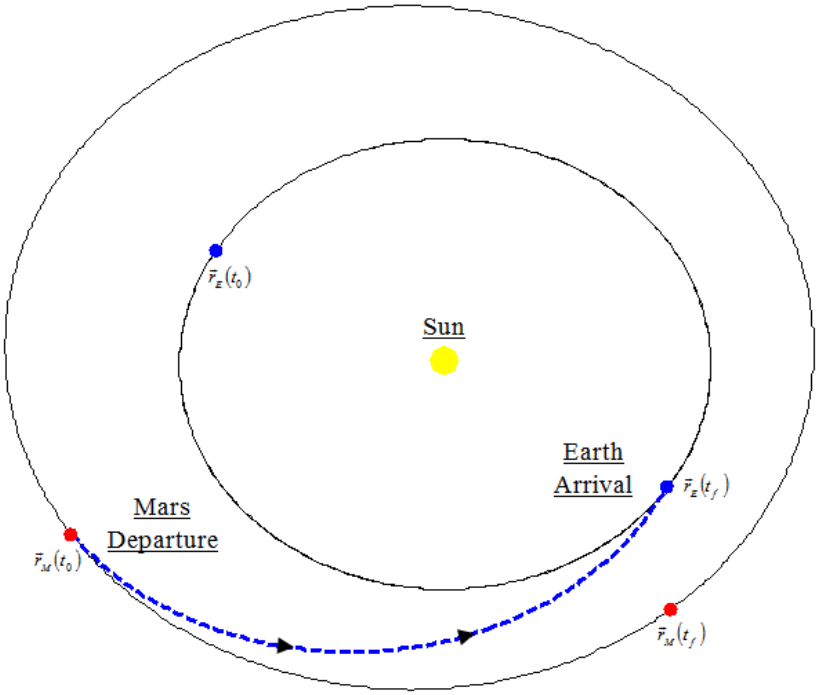

Fig. 6.5 Optimum Mars-to-Earth transfer for Case E.

In order to assess the accuracy calculated optima, it is desirable to compare optimization results to published trajectories. The trajectories in cases A-D and G-H can

be compared to data from NASA's Interplanetary Mission Design Handbook (IMDH) which uses the MIDAS patched-conic trajectory optimization program and coplanar injection maneuvers [24] similar to MMTOP. The IMDH states that the optimal type 1 Earth-to-Mars trajectory in 2026, identical to the conditions specified by case A in this study, has T_0 =[11 14 2026], TOF_1=268 days, and C_3=11.1 km^2/s^2:

Although the C_3 values from MMTOP and the IMDH differ by a non-negligible amount, the similarities between the two studies' T_0 and TOF_1 solutions indicate agreement on the general location of the optimum. The three-day discrepancy between solutions can possibly be explained by the MMTOP assumptions introduced in sections 2.4-2.5 or the use of different planet ephemerides. MIDAS and MMTOP both calculate planet states analytically from ephemerides, but the IMDH does not specify which particular set of ephemerides it uses. NASA has published several sets of ephemerides over the past decade, some more accurate than others [50].

Unfortunately, no suitable publications were found to validate the MMTOP model for cases E-F. Several resources, such as a NASA Johnson Space Center Exploration Office study [25], give energies and entry speeds for round trip Mars missions, but the bounds placed on trajectories do not coincide with the bounds considered for this study. [24] gives an optimal C_3=20.90 km^2/s^2 for a 180-day Earth-to-Mars transfer but allows a Mars V_{EI} =7.76 km/s, well above the 6 km/s limit imposed in this study. Such inconsistencies prevent direct comparison of the physical models of each study.

While unable to validate the physical model for cases E-F, optimization routine effectiveness can be demonstrated by comparing the solution space mapping in Figs. 6.6-6.8 with the MMTOP optima given in Table 6.4. Figure 6.6 maps the IMLEO values of

the minimum IMLEO and ΔV solutions for trajectories with 180-day transfers, $T_{stay} = [0,2500]$ days, and T_0 allowed to vary on the range [250,450]. Figure 6.7 shows an enlarged view of the global minima region from Fig. 6.6, and Fig. 6.8 shows ΔV values of the same region. The global minima in Fig. 6.6-6.8 are the same as the MMTOP optima given in Table 6.4, thus verifying the algorithm's success.

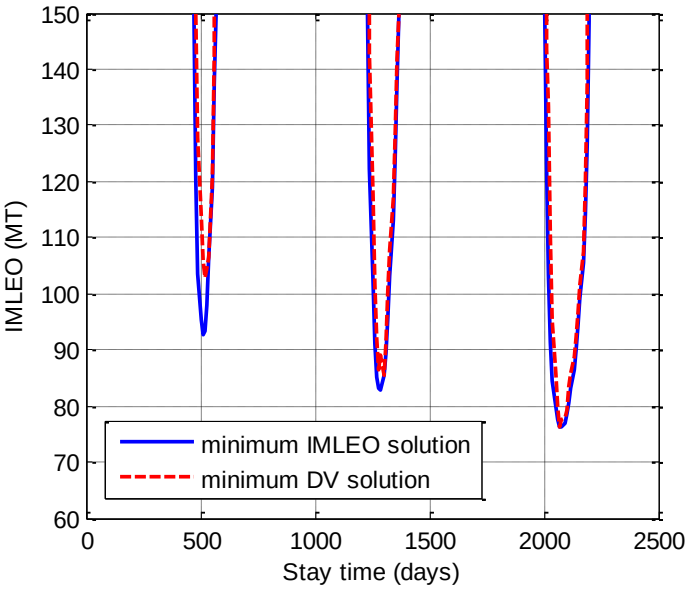

Fig. 6.6 IMLEO **of minimized** IMLEO **and total** ΔV **missions with 180-day transfers.**

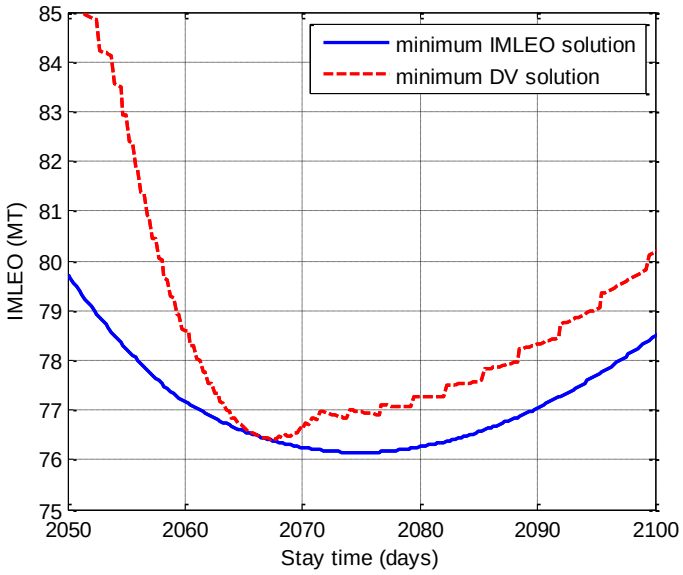

Fig. 6.7 IMLEO **of minimum** IMLEO **and minimum** ΔV **solutions with 180-day transfers.**

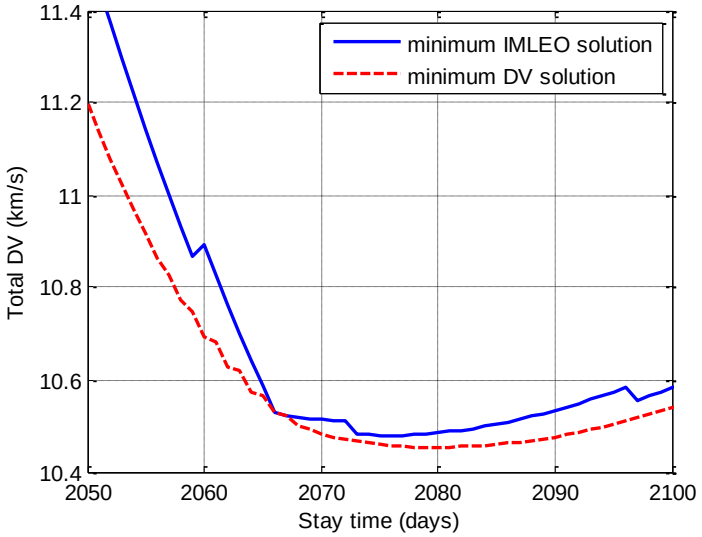

Fig. 6.8 ΔV **of minimum** IMLEO **and minimum** ΔV **solutions with 180-day transfers.**

6.3 DE Optimization Results

Several operations in the DE routine rely on random uniform distributions, and consequently, the optimization results of a series of trials are not typically identical. [31]

showed that results of separate 1000-trial runs are sufficiently similar, so the 1000-trial strategy is used here in all but cases E-F. Unfortunately, due to an error found late in the compilation of this study, trials for cases E-F had to be repeated with only 100 trials per run. While the limited run number decreases statistical accuracy, the results still give indications of the general performance.

Optimizations are run for each tuning parameter configuration and mission case. Depending on the effectiveness of a given tuning parameter configuration, results of each set of 1000 trials can be characterized in several different ways. Figures 6.8-6.10 show several typical outcomes. Figure 6.8 shows results for a parameter configuration with good convergence: A large number of solutions are clustered near the best-known optimum.

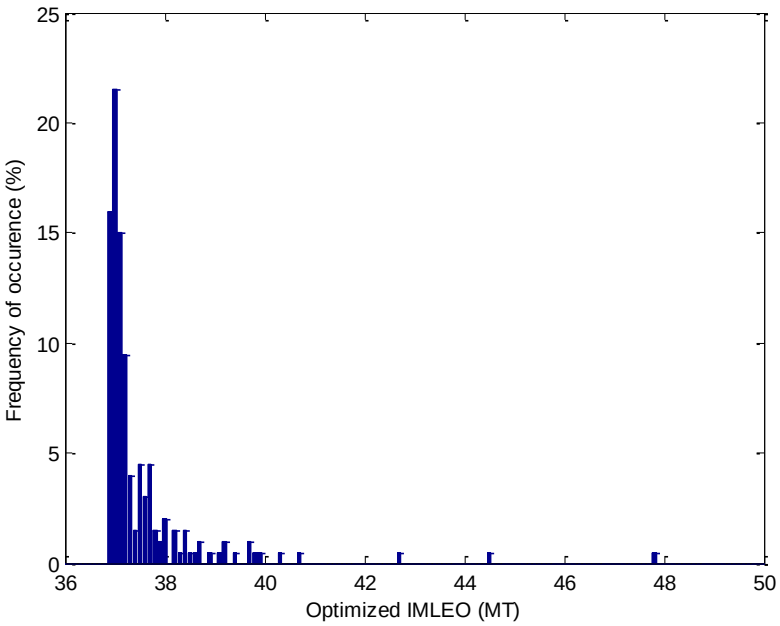

Fig. 6.9 Histogram of IMLEO results for 1000 runs on case D with *CR*=0.2 and *NP*=30.

The clustering near the optimum indicates that many trials successfully find the general location of the optimum but do not fully converge on it. Table 6.6 shows that these

solutions may be very close to the $\vec{x}_{opt}$ as only minor deviations from $\vec{x}_{opt}$ can result in significant increases in IMLEO and ΔV.

Table 6.6 Sensitivity of objective functions to minor deviations from optimal design variation.

T_0 (*mo., day, year*)	TOF_1 (days)	T_{stay} (days)	TOF_2 (days)	IMLEO (kg)	Total ΔV (km/s)
[11 11 2026]	271.57	1998.16	217.45	36,926	7.8580
[11 12 2026]	270.57	1998.16	217.45	37,099	7.8874
[11 13 2026]	269.57	1998.16	217.45	37,208	7.9004
[11 14 2026]	268.57	1988.16	217.45	37,321	7.9133
[11 11 2026]	271.57	1998.16	216.45	36,927	7.8582
[11 11 2026]	271.57	1998.16	215.45	36,930	7.8587

Figure 6.9 shows typical optimization results for poor tuning parameters. In this case, MMTOP fails to converge on the true optimum (see Table 6.6) in any trial, but a large number of trials converge on a local minima.

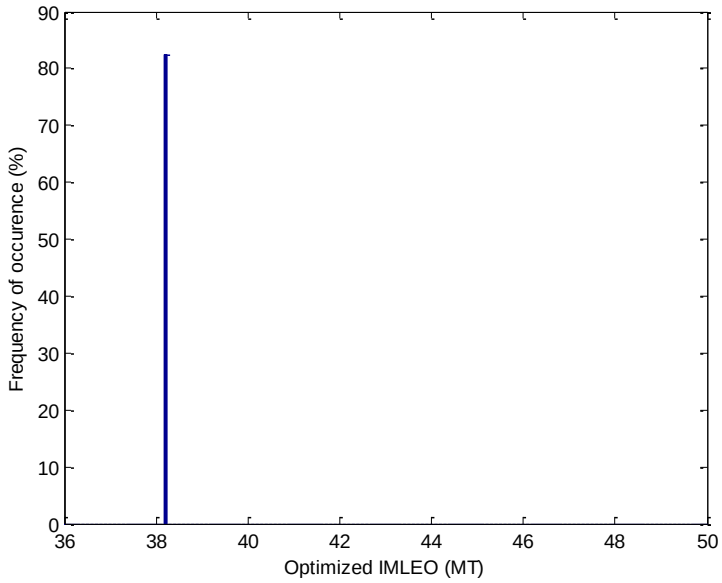

Fig. 6.10 Histogram of results for 1000 runs on case D with *CR*=0.8 and *NP*=20.

Figure 6.10 shows results for a set of trials that completely fail to optimize to the problem.

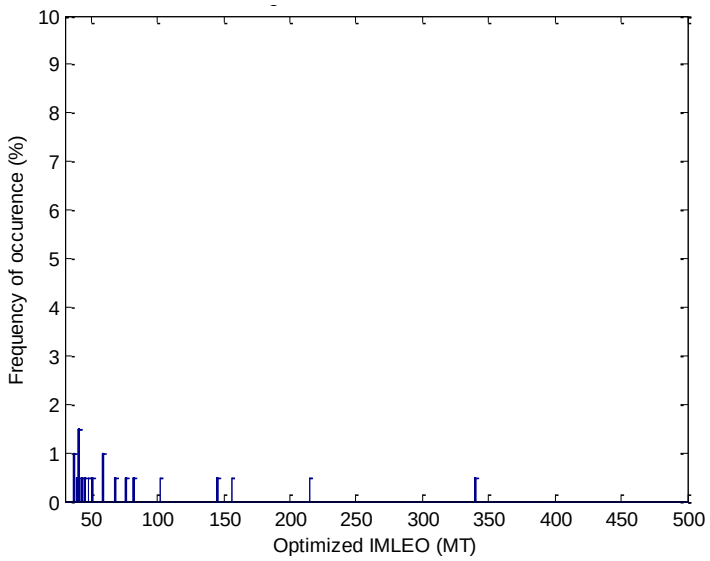

Fig. 6.11 Histogram of results for 1000 runs on case D with *CR*=1 and *NP*=10.

Tables 6.7-6.22 present results for each design case. Criteria D1 and D3 are applied to ΔV optimizations, and criteria D2 and D3 are applied to IMLEO optimizations. With each criterion, performance of each set of tuning parameters can largely be judged by the time per trial T_{trial} and the success rate P_S. To combine the two terms into a more useful performance parameter we introduce $T_{95\%}$, the time required to optimize to a 95% confidence level. The 95% confidence time is given by

$$T_{95\%} = T_{trial} \frac{\log(1-0.95)}{\log(1-P_S)} \tag{6.1}$$

The best parameter configurations yield low T_{trial}, high P_S, and thus low $T_{95\%}$.

Tables 6.7-6.8 give the performance for case A optimization for total ΔV over a 32-year launch window. To reliably optimize to the minimum total ΔV, MMTOP requires a minimum of 18.13 minutes; however, the D3 criterion is met with 95% confidence in just 2.12 minutes.

Table 6.7 Performance data for case A with success criteria D1.

CR	*NP* = 10	*NP* = 20	*NP* = 30	*NP* = 40
Frequency of success (%)				
0.2	1.9	-	-	-
0.4	2.7	1.4	0.9	1.0
0.6	1.6	1.7	-	-
0.8	0.9	2.2	-	-
1	-	-	0.7	-
Average time per trial (s)				
0.2	11.7	20.1	27.4	36.4
0.4	9.8	19.9	29.8	39.7
0.6	10.0	19.9	29.8	40.6
0.8	10.0	19.9	29.8	39.8
1	10.4	21.5	29.8	39.5
95% confidence time (min)				
0.2	30.97	-	-	-
0.4	18.13	70.00	161.14	203.46
0.6	31.12	57.30	-	-
0.8	53.60	45.08	-	-
1	-	-	212.09	-

Table 6.8 Performance data for case A with success criteria D3.

CR	*NP* = 10	*NP* = 20	*NP* = 30	*NP* = 40
Frequency of success (%)				
0.2	4.7	2.9	1.2	5.0
0.4	20.6	20.0	25.4	30.5
0.6	12.9	25.3	25.5	31.3
0.8	6.1	22.1	20.6	31.4
1	-	0.9	4.3	13.7
95% confidence time (min)				
0.2	12.09	33.76	110.34	35.70
0.4	2.12	4.44	5.09	5.46
0.6	3.61	3.41	5.06	5.39
0.8	7.98	3.97	6.44	5.28
1	-	118.85	34.06	13.38

Tables 6.9-6.10 give the performance for case B. Reliably optimizing for minimum IMLEO over the 32-year timeframe requires 18.95 minutes, but locating the general area of the optimum only requires 2.21 minutes.

Table 6.9 Performance data for case B with success criteria D2.

CR	*NP* = 10	*NP* = 20	*NP* = 30	*NP* = 40
Frequency of success (%)				
0.2	-	-	-	-
0.4	2.6	3.1	3.8	3.9
0.6	1.4	0.8	-	-
0.8	-	-	-	-
1	-	-	1.3	-
Average time per trial (s)				
0.2	10.5	19.3	28.5	39.4
0.4	10.0	20.0	30.4	46.2
0.6	10.2	20.9	31.6	42.3
0.8	10.4	20.5	30.5	40.9
1	10.3	20.2	30.6	41.2
95% confidence time (min)				
0.2	-	-	-	-
0.4	18.95	31.24	38.79	57.88
0.6	36.85	125.14	-	-
0.8	-	-	-	-
1	-	-	117.63	-

Table 6.10 Performance data for case B with success criteria D3.

CR	*NP* = 10	*NP* = 20	*NP* = 30	*NP* = 40
Frequency of success (%)				
0.2	0.7	-	-	-
0.4	20.2	31.4	32.1	42.9
0.6	8.6	24.3	38.3	52.7
0.8	2.3	14.1	29.3	29.5
1	-	-	6.1	13.0
95% confidence time (min)				
0.2	72.76	-	-	-
0.4	2.21	2.65	3.93	4.13
0.6	5.64	3.75	3.26	2.82
0.8	22.30	6.73	4.38	5.84
1	-	-	24.18	14.80

Tables 6.11-6.12 detail performance for case C. Here, the design space is restricted to a single 2.1-year synodic period. The smaller design space naturally yields

superior convergence to case A. Case C has a minimum $T_{95\%} = 4.56$ minutes for ΔV but a much lower $T_{95\%} = 0.38$ minutes for optimizing with criterion D3.

Table 6.11 Performance data for case C with success criteria D1.

CR	*NP* = 10	*NP* = 20	*NP* = 30	*NP* = 40
Frequency of success (%)				
0.2	7.2	19.0	19.4	23.6
0.4	9.7	12.3	0.6	-
0.6	7.0	3.5	-	-
0.8	5.8	8.6	-	-
1	-	1.4	9.2	5.1
Average time per trial (s)				
0.2	10.3	19.9	28.2	37.5
0.4	9.4	18.7	28.0	37.7
0.6	10.6	19.9	28.2	39.9
0.8	9.8	19.5	29.7	40.4
1	9.9	19.7	29.7	42.1
95% confidence time (min)				
0.2	6.85	4.74	6.56	6.94
0.4	4.56	7.11	240.48	-
0.6	7.36	27.82	-	-
0.8	8.21	10.83	-	-
1	-	69.24	15.32	40.27

Table 6.12 Performance data for case C and success criteria D3.

CR	*NP* = 10	*NP* = 20	*NP* = 30	*NP* = 40
Frequency of success (%)				
0.2	38.8	61.3	68.1	79.3
0.4	52.7	91.4	99.6	100
0.6	35.0	82.2	92.1	97.4
0.8	20.1	72.1	84.2	86.9
1	-	6.5	36.8	64.0
95% confidence time (min)				
0.2	1.04	1.05	1.23	1.19
0.4	0.62	0.38	0.47	0.63
0.6	1.23	0.57	0.56	0.55
0.8	2.18	0.77	0.80	0.99
1	-	14.56	3.23	2.05

Similar to the relationship between cases A and C, case D convergence is superior to B, locating the area of the general solution in just 0.66 minutes. Note in Table 6.13, however, that IMLEO optimization for case D requires $T_{95\%} = 7.01$ minutes as opposed to $T_{95\%} = 4.56$ minutes for the case C ΔV optimization.

Table 6.13 Performance data for case D with success criteria D2.

CR	*NP* = 10	*NP* = 20	*NP* = 30	*NP* = 40
Frequency of success (%)				
0.2	3.6	6.8	17.5	11.2
0.4	5.8	7.1	1.6	0.7
0.6	5.2	2.7	0.6	-
0.8	4.5	-	-	-
1	-	0.8	12.5	4.5
Average time per trial (s)				
0.2	9.2	18.0	26.9	37.0
0.4	10.1	20.6	30.2	39.8
0.6	9.8	19.6	29.5	39.3
0.8	9.9	19.6	29.5	39.3
1	9.8	19.6	29.6	43.1
95% confidence time (min)				
0.2	12.58	12.73	7.01	15.54
0.4	8.38	13.89	95.92	278.99
0.6	9.16	35.69	240.77	-
0.8	10.70	-	-	-
1	-	126.69	11.06	46.73

Table 6.14 Performance data for case D and success criteria D3.

CR	*NP* = 10	*NP* = 20	*NP* = 30	*NP* = 40
Frequency of success (%)				
0.2	31.4	40.2	52.7	54.1
0.4	52.7	80.7	90.7	98.8
0.6	28.2	68.4	80.8	90.2
0.8	15.4	53.0	72.8	82.7
1	-	4.8	30.7	65.3
95% confidence time (min)				
0.2	1.62	2.34	2.40	3.17
0.4	0.90	0.83	0.84	0.66
0.6	1.99	1.15	1.20	1.14
0.8	3.94	1.75	1.51	1.49
1	-	27.32	5.34	2.71

Cases E-F present some analysis difficulties, as there is no standard for validation of model accuracy. Due to lack of literature sources that use similar trajectory bounds, Tables 6.15-6.18 should only be regarded as measuring the DE routine's effectiveness with the adopted physical model. The optima used for success definitions are taken from Fig. 6.5-6.7. Using these definitions, Tables 6.15-6.18 show exceptional convergence with P_S =100% and optimization to 95% confidence in just 9 seconds.

Table 6.15 Performance data for case E with success criteria D1.

CR	*NP* = 10	*NP* = 20	*NP* = 30	*NP* = 40
Frequency of success (%)				
0.2	100	100	100	100
0.4	92	100	100	100
0.6	72	100	100	100
0.8	93	100	100	100
1	-	-	18	59
Average time per trial (s)				
0.2	9.2	17.9	26.9	35.6
0.4	9.0	18.0	26.9	35.8
0.6	9.0	17.9	26.9	35.6
0.8	8.9	17.9	26.7	35.6
1	9.0	17.9	26.8	35.8
95% confidence time (min)				
0.2	0.15	0.30	0.45	0.59
0.4	0.18	0.30	0.45	0.60
0.6	0.35	0.30	0.45	0.59
0.8	0.17	0.30	0.45	0.59
1	-	-	6.75	2.00

Table 6.16 Performance data for case E and success criteria D3.

CR	*NP* = 10	*NP* = 20	*NP* = 30	*NP* = 40
Frequency of success (%)				
0.2	100	100	100	100
0.4	100	100	100	100
0.6	100	100	100	100
0.8	100	100	100	100
1	18	32	75	93
95% confidence time (min)				
0.2	0.15	0.30	0.45	0.59
0.4	0.15	0.30	0.45	0.60
0.6	0.15	0.30	0.45	0.59
0.8	0.15	0.30	0.45	0.59
1	2.25	2.31	0.97	0.67

Table 6.17 Performance data for case F with success criteria D2.

CR	*NP* = 10	*NP* = 20	*NP* = 30	*NP* = 40
Frequency of success (%)				
0.2	90	100	100	100
0.4	100	100	100	100
0.6	100	100	100	100
0.8	53	100	100	100
1	-	9	44	61
Average time per trial (s)				
0.2	9.6	78.8	27.2	36.5
0.4	9.2	18.1	27.1	36.1
0.6	9.1	18.1	27.1	36.1
0.8	9.2	18.1	27.2	36.0
1	90.0	18.0	27.0	36.0
95% confidence time (min)				
0.2	0.21	0.31	0.45	0.61
0.4	0.15	0.30	0.45	0.60
0.6	0.15	0.30	0.45	0.60
0.8	0.60	0.30	0.45	0.60
1	-	9.53	2.32	1.91

Table 6.18 Performance data for case F and success criteria D3.

CR	*NP* = 10	*NP* = 20	*NP* = 30	*NP* = 40
Frequency of success (%)				
0.2	100	100	100	100
0.4	100	100	100	100
0.6	100	100	100	100
0.8	68	100	100	100
1	-	63	75	100
95% confidence time (min)				
0.2	0.16	0.31	0.45	0.61
0.4	0.15	0.30	0.45	0.60
0.6	0.15	0.30	0.45	0.60
0.8	0.40	0.30	0.45	0.60
1	-	0.90	0.97	0.60

Tables 6.19-6.20 give the performance of cases G-H. The favorable P_S and $T_{95\%}$ again suggest the potential of using narrow-bounded optimizations after runs with large design spaces as discussed in section 6.2: The $\vec{x}_{opt}$ from large design spaces, such as

those in cases A-D, yield values from which $\vec{x}_{lb}$ and $\vec{x}_{ub}$ can be constructed for rapid, narrow-bounded optimizations similar to cases G-H. Evidencing the rapid convergence in such optimizations, case G optimization to minimum total ΔV only requires $T_{95\%}$ =0.88 minutes, and case H optimization of IMLEO requires $T_{95\%}$ =0.90 minutes.

Table 6.19 Performance data for case G with success criteria D1.

CR	*NP* = 10	*NP* = 20	*NP* = 30	*NP* = 40
Frequency of success (%)				
0.2	42.9	36.4	7.3	-
0.4	6.8	-	-	-
0.6	48.4	-	-	-
0.8	27.5	-	-	-
1	15.2	26.1	8.5	-
Average time per trial (s)				
0.2	9.8	18.1	27.5	38.0
0.4	9.5	19.0	28.5	39.5
0.6	9.7	19.4	29.1	39.7
0.8	9.7	19.3	29.0	38.6
1	9.6	19.3	28.9	38.6
95% confidence time (min)				
0.2	0.88	2.00	18.06	-
0.4	6.73	-	-	-
0.6	0.73	-	-	-
0.8	1.50	-	-	-
1	2.92	3.19	16.20	-

Table 6.20 Performance data for case H with success criteria D2.

CR	*NP* = 10	*NP* = 20	*NP* = 30	*NP* = 40
Frequency of success (%)				
0.2	40.1	35.6	7.0	-
0.4	6.8	-	8.4	-
0.6	23.7	-	-	-
0.8	27.1	7.4	-	-
1	32.7	24.1	20.3	-
Average time per trial (s)				
0.2	9.3	18.3	27.6	36.6
0.4	9.8	19.7	29.6	39.3
0.6	9.8	19.9	29.4	39.1
0.8	9.8	19.6	29.3	39.4
1	9.7	20.1	30.0	39.1
95% confidence time (min)				
0.2	0.90	2.07	18.91	-
0.4	7.00	-	16.81	-
0.6	1.81	-	-	-
0.8	1.56	12.71	-	-
1	1.22	3.64	6.61	-

Table 6.21 gives the best P_S and $T_{95\%}$ achieved for each optimization case and performance criteria. Cases A-B prove the most difficult to optimize because of the larger design space; however, MMTOP reliably locates the basin of attraction in 2.12 minutes and 2.21 minutes when optimizing for ΔV and IMLEO, respectively. Further, the narrow-bounded cases G-H reliably optimize ΔV and IMLEO in 0.73 and 0.90 minutes, respectively. Again, pairing optimizations over the bounds in cases A-B with narrow-bounded trials like cases G-H, the global minimum energy trajectory in a 32-year launch window can be found in just 2.85 minutes when optimizing for ΔV and 3.11 minutes when optimizing IMLEO. If only optimizing over a 3-year launch window, then the optima are found in 1.09 and 1.56 minutes, respectively.

Table 6.21 Best results of all design space cases and success criteria.

Performance measure	Case	D1	D2	D3
P_S (%)	**A**	2.7	-	31.4
	B	-	3.9	52.7
	C	23.6	-	100
	D	-	17.5	98.8
	E	100	-	100
	F	-	100	100
	G	48.4	-	-
	H	-	40.1	-
$T_{95\%}$ (min)	**A**	18.13	-	2.12
	B	-	18.95	2.21
	C	4.56	-	0.38
	D	-	7.01	0.66
	E	0.15	-	0.15
	F	-	0.15	0.15
	G	0.73	-	-
	H	-	0.90	-

Table 6.22 gives the tuning parameter configurations that correspond to the $T_{95\%}$ results in Table 6.21. The settings NP=10 and CR=0.4 generally—but not always—yield the best performance.

Table 6.22 Best tuning parameter configurations for all design spaces and success criteria.

Tuning parameter	Case	D1	D2	D3
NP	**A**	10	-	10
	B	-	10	10
	C	10	-	20
	D	-	30	40
	E	10	-	10
	F	-	10	10
	G	10	-	-
	H	-	10	-
CR	**A**	0.4	-	0.4
	B	-	0.4	0.4
	C	0.4	-	0.4
	D	-	0.2	0.4
	E	0.2	-	0.2
	F	-	0.4	0.4
	G	0.6	-	-
	H	-	0.2	-

The tuning parameter data in Table 6.22 disagrees with [31] that *CR*=0.6 yields the best results for a round-trip Mars mission, and *CR*=0.8 produces the best convergence overall. The disagreement can possibly be explained by two differences in analysis methods: Olds et al. only tested one trajectory problem with *CR*=0.4, and the problems tested generally had more than four design variables. [31] also concluded that *NP*=28 was best for Mars missions, while this thesis found that the much lower *NP*=10 provided the fastest reliable convergence.

CHAPTER 7: CONCLUSION

By combining the performance of test-proven nuclear thermal rockets, modern developments in fuel fabrication, a simplified solar system model, and the stochastic Differential Evolution optimization routine, a Mars sample return mission is designed and optimized. The mission plan develops and flight-proves nuclear thermal rockets—which enable human exploration past the moon—at the relatively low cost of $100 million and completes a major goal of the U.S. space program. To aid mission design, the DE-based MMTOP is constructed to be a robust, efficient optimization tool for preliminary trajectory/mission planning. In order to characterize performance capabilities and make MMTOP more useful for future mission planning, a thorough study of tuning parameters' effects on convergence is conducted for constrained and unconstrained trajectories.

Pairing the extensive engineering knowledge gained from the NERVA program with modernized fuels, a $700 million plan is presented for developing a Pewee-derived NTR. The engine uses W-Re cermet fuel and is implemented on the near-term MSR mission as outlined by the 2010 PSDS. Because the Pewee-derived engine roughly doubles the performance of the best chemical propulsion systems of today, using the NTR for TMI decreases IMLEO requirements to 36.9 MT: The roughly 10 MT decrease in IMLEO from the PSDS architecture thus allows the NTR-augmented mission to employ a single SpaceX Falcon Heavy launch vehicle as opposed to the PSDS's three Altas V's. The resulting $600 million savings in launch costs thus pays for the majority of the Pewee-derived NTR development.

MMTOP uses penalty methods and several physical model approximations to facilitate rapid, practical optimization. The patched-conic and zero sphere of influence dynamics models allow rapid trajectory computation with accuracy sufficient for preliminary planning. After the initial trajectory computation, penalty functions are applied in order to make constraint-violating solutions appear artificially costly during the DE selection process; in this way, MMTOP disallows optimization to infeasible and impractical trajectories. Benchmarking with JPL's QUICK software shows that both the physical model and optimization routine of MMTOP are capable of producing results that are practically identical to industry optimization software.

A thorough study of the effects of the main DE tuning parameters *CR* and *NP* found the overall—but not universally—best configuration for round-trip Mars missions has *CR*=0.4 and *NP*=10. These results disagree with conclusions of Olds et al. that *CR*=0.6 and *NP*=28 yield the best convergence for Mars missions. Discrepancies can be traced to differences in parking orbit specification and problem definition, but this further proves the idea that the effectiveness of a given tuning parameter configuration is highly dependent on the problem being solved.

Running optimizations on a 3.2 GHz Intel i5 processor, CPU time is approximately equal to *NP* for DE runs of 1000 generations. The best results achieved for each trajectory problem have success rates ranging 2.7-100% for direct optimization of the objective function and success rates of 31.4-100% for locating the basin of attraction of the global optima. Generally, smaller design spaces yield much better convergence. Using this knowledge, a strategy of conducting two MMTOP optimizations in series is proposed for fast, reliable optimization of large design spaces:

1) Run MMTOP once over the entire design space to locate the basin of attraction. 2) Run MMTOP a second time with narrow design space bounds that are defined by the results of the first run. In this manner, MMTOP reliably optimizes ΔV in 1.09 minutes and IMLEO in 1.56 minutes for a 3-year launch window. For a 32-year launch window, ΔV and IMLEO are reliably optimized in 2.85 and 3.11 minutes, respectively.

While this study attempts to address the most major issues in mission design and DE trajectory optimization, there are still ways that MMTOP and the given mission design can be improved. For future mission designs, the author advises specifying detailed parking orbit parameters, landing site latitudes, and other similar trajectory conditions, as such considerations can require propulsive burns that were not considered in this study. For future implementation of MMTOP, convergence could potentially be improved by using alternate DE differencing schemes, larger maximum generation numbers, and adaptive parameter control methods: The latter two options actually increase optimization time, but the algorithm robustness increases as well. In optimizations of unknown design spaces, the importance of robustness greatly outweighs that of optimization time.

REFERENCES

1. Cooper, R.S., 1968, "Nuclear Propulsion for Space Vehicles," *Annual Review of Nuclear Science*, **18**, pp. 203-228.

2. Bowles, M.D., Arrighi, R.S., 2004, "NASA's Nuclear Frontier: The Plum Brook Reactor Facility," *Monographs in Aerospace History*, **33**.

3. Griffin, M.D., French, J.R., 2004, *Space Vehicle Design*, American Institute of Aeronautics and Astronautics.

4. Robbins, W.H., Finger, H.B., 1991, *An Historical Perspective of the NERVA Nuclear Rocket Engine Technology Program*, NASA Lewis Research Center.

5. NASA Earth Science and Technology Office, *Definition of Technology Readiness Levels*, http://esto.nasa.gov/files/TRL_definitions.pdf, (12 Oct. 2011).

6. Dewar, J.A., 2008, *To the End of the Solar System*, Collector's Guide Publishing Inc., Burlington, ONT.

7. Howe, S.D., 2010, "Mars Hopper: A Radioisotope Powered, Long-Lived, Long-Range Mobil Platform Using In-situ Resources," *56th JANNAF Propulsion Meeting*.

8. Merkle C., 1999, "Ad Astra per Aspera: Reaching for the Stars," Report of the Independent Review Panel of the NASA Space Transportation Research Program.

9. Mars Architecture Steering Group, 2009, *Human Exploration of Mars Design Reference Architecture 5.0*, NASA.

10. Borowski S.K., 1991, *The Rationale/Benefits of Nuclear Thermal Rocket Propulsion for NASA's Lunar Space Transportation System*, NASA Technical Memorandum 106739, AIAA-91-2052.

11. Hickman R., Panda B., Shah S., 2005, "Fabrication of High Temperature Cermet Materials for Nuclear Thermal Propulsion," *53rd JANNAF Propulsion Meeting*.

12. Joyner, C.R., Phillips, J.E., Fowler, R.B., Borowski, S.K., 2004, "TRITON: A TRImodal Capable, Thrust Optimized, Nuclear Propulsion and Power System for Advanced Space Mission," *40th Joint Propulsion Conference*.

13. Houts, M.G., 2011, *Advanced Exploration Systems Nuclear Cryogenic Propulsion Stage (NCPS)*, Workshop on Future Directions for Space Nuclear Power and Propulsion, Idaho Falls, ID.

14. Allen, R.E., Manning, B.T., Chlapek, T.C., Howe. S.D., 2011, "Preliminary Mission Architecture for Mars Sample Return Utilizing Nuclear Thermal Rockets," *Proceedings of Nuclear and Emerging Technologies for Space 2011*, Paper 3291.

15. Howe, S.D., 2005, *Identification of Archived Design Information on Small Class Nuclear Rockets*, Los Alamos National Laboratory.

16. Howe, S.D., Travis, B., Zerkle, D.K., 2003, "SAFE Testing Nuclear Rockets Economically," *Space Technology and Applications International Forum*.

17. Chang K., 2010, "NASA Gets New Orders That Bypass the Moon," *The New York Times*, A16, (1 Oct. 2010).

18. Squyres S., 2011, "Visian and Voyages for Planetary Science in the Decade 2013-2022", *42nd Lunar and Planetary Science Conference*.

19. Svitak A., *U.S., Europe Plan Single-rover Mars Mission for 2018*, 18 Apr. 2011, http://www.spacenews.com/civil/110418-single-rover-mars-mission-2018.html, (1 Oct. 2011).

20. Syvertson, M., 2010, *Planetary Science Decadal Survey Mars 2018 MAX-C Caching Rover*, NASA, Pasadena, CA.

21. Space Exploration Technologies, *Falcon Heavy Overview*, 2011, http://www.spacex.com/falcon_heavy.php, (12 June 2011).

22. United Launch Alliance, 2010, *Atlas V Launch Services User's Guide 2010*, (2-29).

23. NASA, 2003, *Mars Exploration Rover Launches Press Kit*, NASA.

24. Burke, L.M., Falck, R.D., McGuire, M.L., 2010, *Interplanetary Mission Design Handbook: Earth-to-Mars Mission Opportunities 2026 to 2045*, NASA Glenn Research Center, Cleveland, OH.

25. Munk, M.M., *Departure Energies, Trip Times, and Entry Speeds for Human Mars Missions*, NASA Johnson Space Center.

26. Matousek, S., Sergeyevsky, A.B., "To Mars and Back: 2002-2020, Ballistic Trajectory Data for the Mission Architect," *AIAA/AAS Astrodynamics Specialist Conference and Exhibit 1998*, pp. 254-264.

27. Storn, R., Price, K., 1997, "Differential Evolution – A Simple and Efficient Heuristic for Global Optimization over Continuous Spaces," *Journal of Global Optimization*, **11**, pp. 341-359.

28. Feoktistov, V., 2006, *Differential Evolution: In Search of Solutions*, Springer, New York, NY.

29. Myatt D.R., Becerra V.M., Nasuto S.J., Bishop J.M., 2004, "Advanced Global Optimization Tools for Mission Analysis and Design," *Final Report of ESA Ariadna ITT* AO4532/18138/04/NL/MV, Call 03/4101.

30. Di Lizia P., Radice G., 2004, "Advanced Global Optimization Tools for Mission Analysis and Design," *Final Report of ESA Ariadna ITT* A04532/18139/04/NL/MV, Call 03/4101.

31. Olds, A.D., Kluever, C.A., Cupples, M., 2007, "Interplanetary Mission Design Using Differential Evolution," *Journal of Spacecraft and Rockets*, **44**, pp. 1060-1070.

32. Sentinella M.R., Casalino L., 2009, "Cooperative Evolutionary Algorithm for Space Trajectory Optimization," *Celestial Mechanicals and Dynamical Astronomy*, **105**, pp. 211-227.

33. Vinkó, T., Izzo, D., Bombardelli, C., 2007, "Benchmarking Different Global Optimisation Techniques for Preliminary Space Trajectory Design," *58th International Astronautical Congress*.

34. Curtis, H., 2005, *Orbital Mechanics for Engineering Students*, Elsevier Butterworth Heinemann, Burlington, MA.

35. Izzo, D., ESA Advanced Concepts Team, *Lambert Solver*, 2007, http://www.esa.int/gsp/ACT/doc/INF/Code/globopt/mga/mga.m, (10 Oct. 2010).

36. Braun R.D., Manning R.M., 2007, "Mars Entry, Descent, and Landing Challenges," *Journal of Spacecraft and Rockets*, **44**, 310-323.

37. Desai, P.N., Knocke, P.C., "Mars Exploration Rovers Entry, Descent, and Landing Trajectory Analysis", *Journal of the Astronautical Sciences*, **55**, pp. 311-323.

38. Sutton, G.P., Biblarz, O., 2010, *Rocket Propulsion Elements*, John Wiley and Sons.

39. Amos J., *US and Europe Mull Single 2018 Mars Rover*, 7 Apr. 2011, http://www.bbc.co.uk/news/science-environment-13002214, (20 Aug. 2011).

40. *Science Objectives of the ExoMars Rover*, 7 Oct. 2011, http://sci.esa.int/science-e/www/object/index.cfm?fobjectid=45082, (28 Oct. 2011).

41. Mattingly, R., 2010, *Planetary Science Decadal Survey MSR Orbiter Mission*, NASA, Pasadena, CA.

42. Mattingly, R., 2010, *Planetary Science Decadal Survey MSR Lander Mission*, NASA, Pasadena, CA.

43. NASA, 2004, *Stardust Comet Flyby*, Pasadena, CA.

44. Joyner, C.R., 2010, *TRITON LANTR Performance*, Pratt Whitney Rocketdyne, (personal communication).

45. Manning, B.T., 2 Aug. 2011, Idaho Falls, ID, (personal communication).

46. Yamaguchi, S., 2011, "An Automatic Control Parameter Tuning Method for Differential Evolution," *Electrical Engineering in Japan*, **174**, pp. 25-33.

47. Tvrdik, J., 2006, "Differential Evolution: Competitive Setting of Control Parameters," *Proceedings of the International Multiconference on Computer Science and Information Technology*, pp. 207-213.

48. Brest, J., Greiner, S., Bocskovic´, B., Mernik, M., Zumer., V., 2006, "Self-Adapting Control Parameters in Differential Evolution: A Comparative Study on Numerical Benchmark Problems", *IEEE Transactions on Evolutionary Computation*, **10**, pp. 646-657.

49. Storn, R., Price, K., *Differential Evolution*, http://www.icsi.berkeley.edu/~storn/code.html, (10 Oct. 2010).

50. Folkner, W., *JPL Planetary and Lunar Ephemerides: Export Information*, 17 Mar. 2011, http://iau-comm4.jpl.nasa.gov/README, (1 Nov. 2011).